nature portfolio

https://doi.org/10.1038/s41563-021-01016-0

Supplementary information

Revealing the role of the cathode–electrolyte interface on solid-state batteries

In the format provided by the authors and unedited

Revealing the role of the cathode-electrolyte interface on solid-state batteries

Beniamin Zahiri[1,3,4], Arghya Patra[1,3,4], Chadd Kiggins[5], Adrian Xiao Bin Yong[1,4], Elif Ertekin[3,6], John B. Cook[5*], Paul V. Braun[1,2,3,4*]

[1]Department of Materials Science and Engineering, University of Illinois at Urbana-Champaign, Urbana, IL 61801, USA

[2]Department of Chemistry, University of Illinois at Urbana-Champaign, Urbana, IL 61801, USA

[3]Materials Research Laboratory, University of Illinois at Urbana-Champaign, Urbana, IL 61801, USA

[4]Beckman Institute for Advanced Science and Technology, University of Illinois at Urbana-Champaign, Urbana, IL 61801, USA

[5]Xerion Advanced Battery Corporation, 3100 Research Boulevard St. 320, Kettering, OH 45420, USA

[6]Department of Mechanical Science and Engineering, University of Illinois at Urbana-Champaign, Urbana, IL, 61801, USA

*corresponding authors: pbraun@illinois.edu, john.cook@xerionbattery.com

Supplementary Information

SI 1. Crystal Shape 3
SI 2. Ion beam SEM imaging 4
SI 3. TEM analysis of as-synthesized faceted LCO 5
SI 4. XRD analysis of dense LCO texture 7
SI 5. Surface roughness analysis based on laser scanning confocal microscopy 10
SI 6. Dense sodium ($NaCoO_2$) cathodes 11
SI 7. Characterization of solid electrolytes 12
SI 7.1. Halide solid electrolytes for Li ion system 12
SI 7.2. Sulphide and halide solid electrolytes for Na ion system 14
SI 8. Liquid cell performance of dense LCOs 15
SI 9. Solid-state cell performance 17
SI 9.1. Dense LCOs vs. composite cathodes 17
SI 9.1.1. Thick LCO SSB testing 25
SI 9.1.2. Impact of LCO loading and cycling rate 26
SI 9.2. Dense NCOs vs. composite cathodes 26
SI 10. GITT analysis 28
SI 11. EIS analysis 28
SI 11.1. Li-ion systems 28
SI 11.1.1. Intra-cycle EIS 28
SI 11.1.2. SE electrochemical stability via EIS intra-cycle test: LYC vs. LIC 33
SI 11.1.3. Inter-cycling EIS tests: 0.2C cycling 33
SI 11.1.4. Inter-cycling EIS tests: 0.1C cycling 34
SI 11.1.5. Inter-cycling EIS tests: 0.5C cycling 35
SI 11.2. Na-ion systems 37
SI 12. Interface Chemistry 38
SI 13. Interface Microstructure 43
SI 14. Energy density calculations: composite vs. dense cathode 45
References 45

SI 1. Crystal Shape

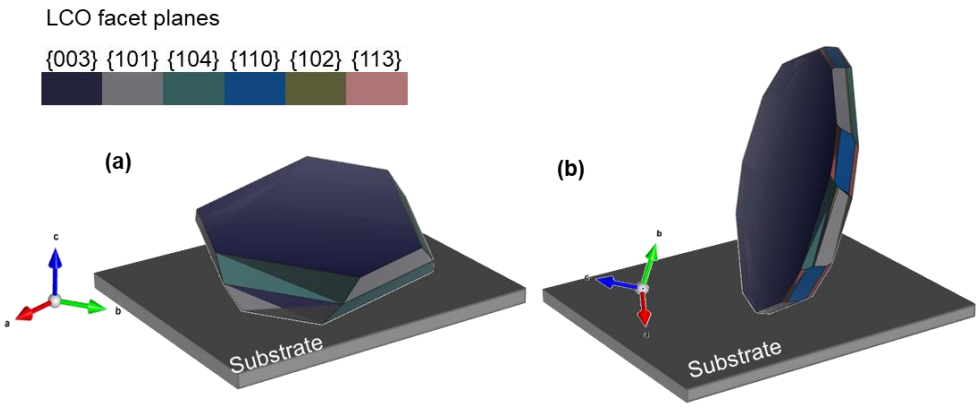

Basal plane platelet Highly/poorly faceted platelet

Figure S1. The shape of crystal reproduced by Vesta for (a) BP LCO and (b) HF and PF LCO platelets showing the range of crystal planes that can exist in the step edges of each platelet (by Vesta[1] crystal visualization software).

SI 2. Ion beam SEM imaging

Channelling contrast[2] in ion-beam induced SEM (i-SEM) imaging reveals details of the nature of the faceting (Figure S2). The contrast in the case of BP LCO (Figure S2 (b)) suggests individual LCO grains are preferentially grown in the <003> direction with a narrow inter-granular void space between neighbouring grains. In contrast, i-SEM for HF LCO (Figure S2 (c and d)) reveals channelling contrast within a single grain. Individual grains show the presence of a core (darker contrast) and a series of tightly bound "branches" extending from central core to the surface. The structure of PF LCO indicates the absence of a central core while the branching behaviour persists (Figure S2 (e and f)).

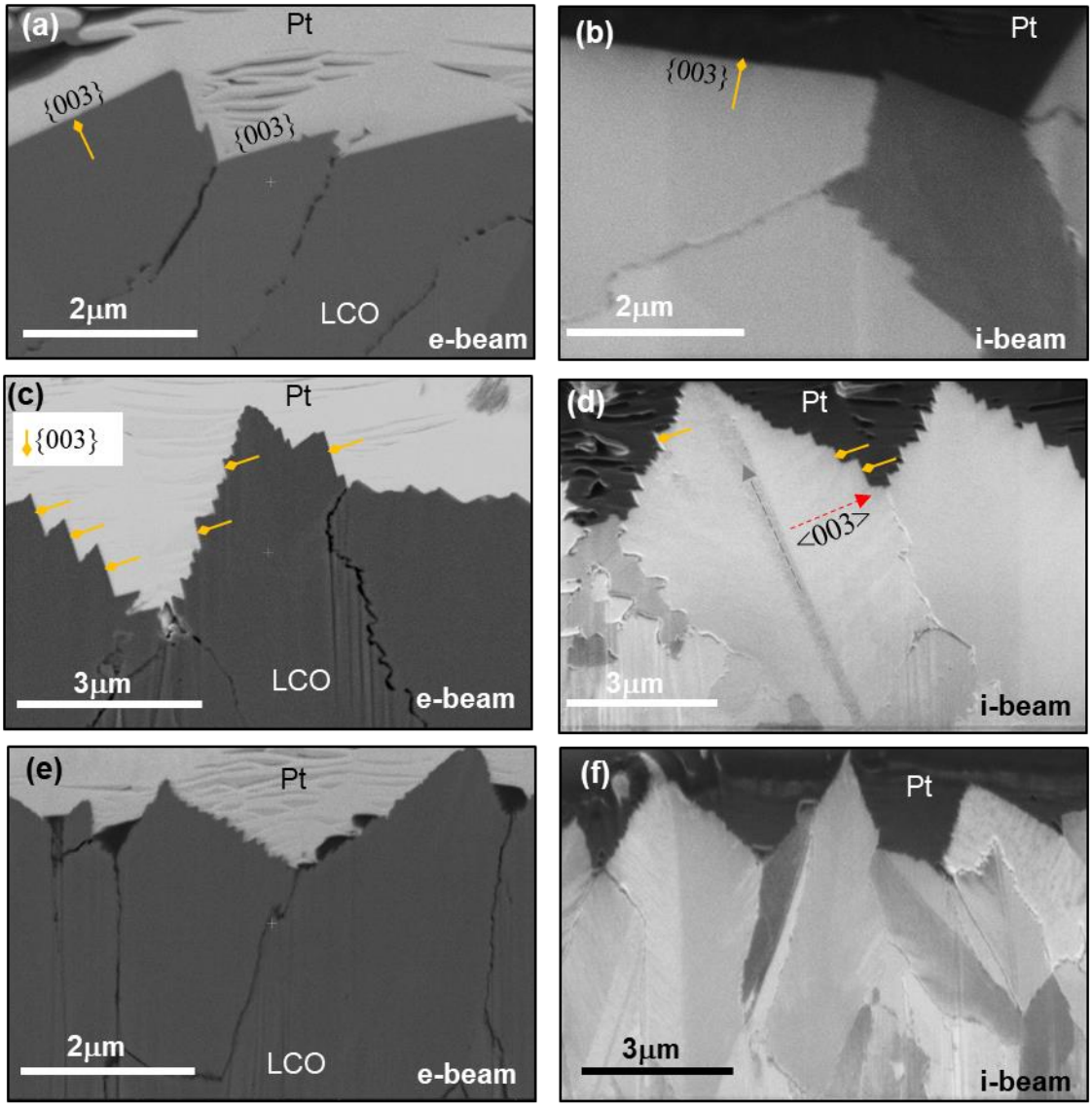

Figure S2. Electron beam and ion beam SEM micrographs for (a,b) BP LCO and (c,d) HF LCO and (e,f) PF LCO cros section. Ion beam SEM depicts channelling contrast due to variation in crystallographic orientation of neighbouring grains and crystal domain. BP LCO (b) shows orientation variation between neighbouring grains while HF and PF LCO (d and f) show inter-granular channelling contrast. HF LCO shows a central core (gray contrast in d) and branch-like structure with (003) faces highlighted by amber arrows.

SI 3. TEM analysis of as-synthesized faceted LCO

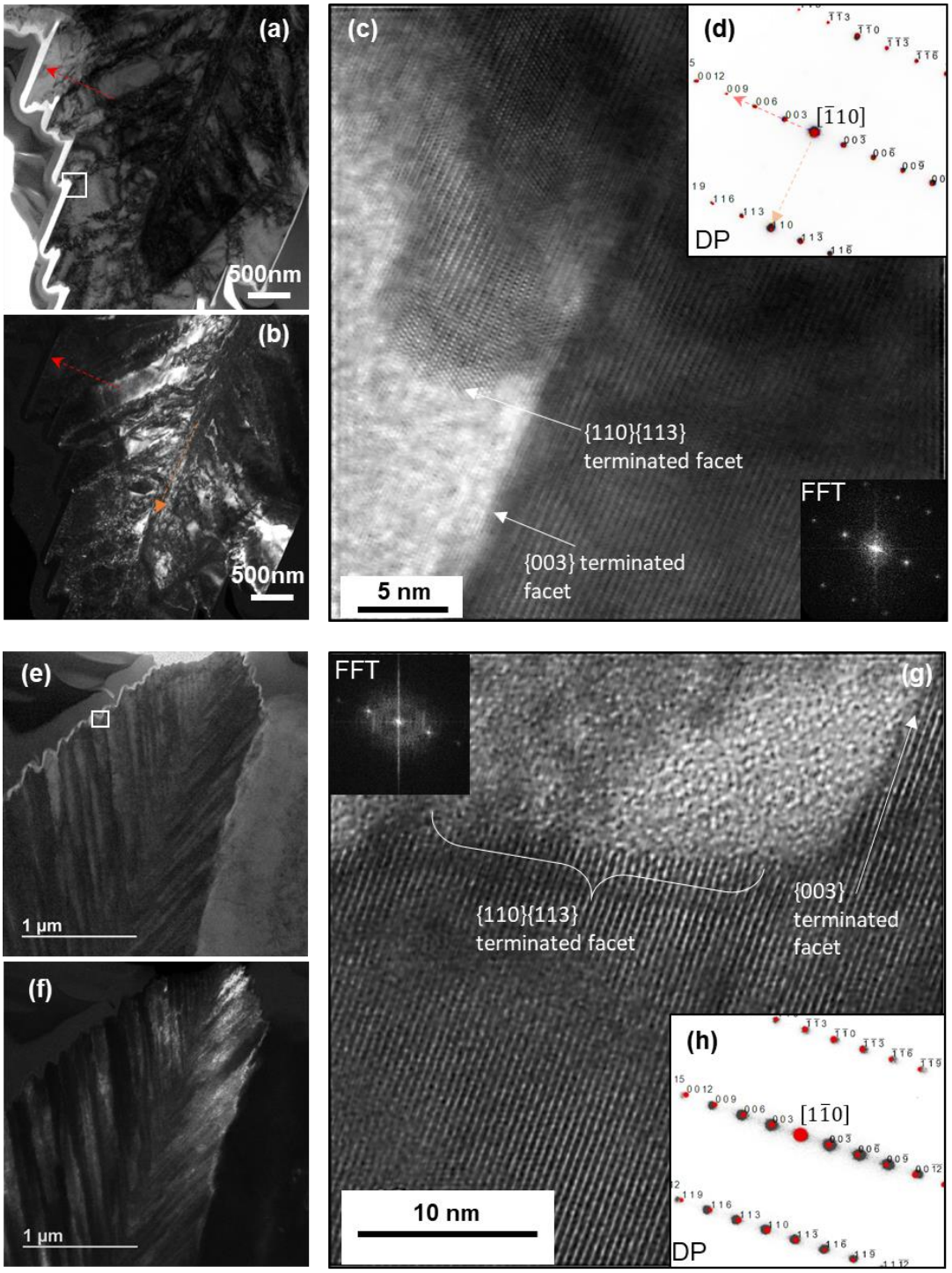

Figure S3. TEM (bright and dark filed), high resolution micrographs and SAED patterns of (a-d) HF LCO and (e-h) PF LCO samples prepared via FIB. The central core and corresponding growth direction <110> are shown by orange dashed arrow. Simulated diffraction pattern overlaid on measured pattern (CrystalMaker). {003} planes are shown by red dashed arrow in (a,b). Dark field micrographs were collected using g = $(003)_{LCO}$ reflection.

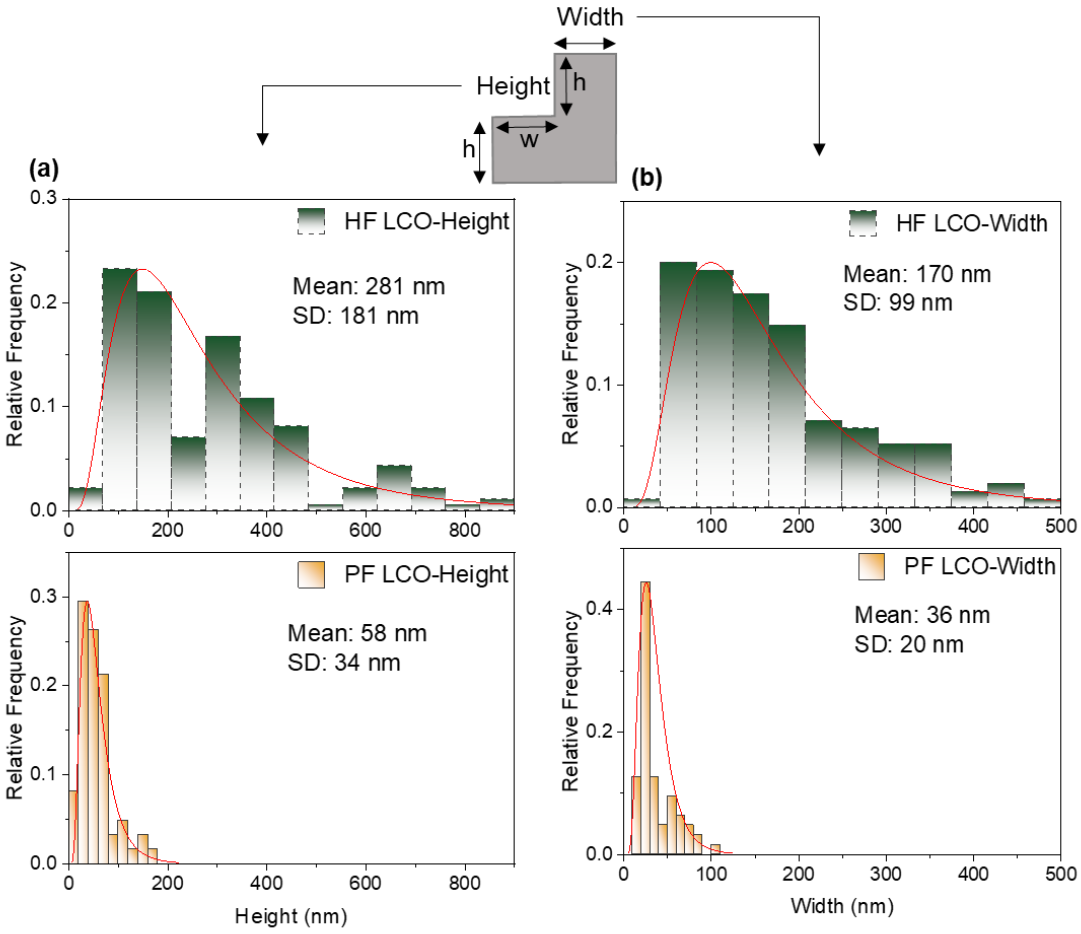

Figure S4. Histograms showing the (a) height and (b) width of terracing steps in cross section SEM and TEM imaging of HF and PF LCOs.

SI 4. XRD analysis of dense LCO texture

XRD confirms the orientation differences between the BP, PF, and HF samples. Figure S5 (a) and Table S1 show strong orientation of BP LCO in <003> direction. The powder LCO (used for composite cathode fabrication) also displays larger 003 contribution than standard LCO structure most likely due to rearrangement of particles during XRD sample preparation. In contrast, HF and PF LCOs show large (>1) texture coefficient values for fast-diffusing facets such as (110) and (101). Texture analysis based on X-ray pole figures from (003), (104), (110) poles is also presented in the form of calculated inverse pole figures in Figure S5 (c-e). A typical stereographic projection of LCO in the basal plane zone axis is also presented as a reference. BP LCO shows strong 003 orientation in the normal to substrate direction representing a {001}<110> (001 || ND, 110 || CD; ND normal direction, CD cross direction) type texture. On the other hand, HF and PF LCO show similar preferred orientation in 110 facets with a dominant {110}<001> type texture. Higher multiples of random distribution (mrd) for HF LCO is in line with wider terrace steps. Surface roughness, analysed by laser scanning confocal microscopy (Figure S6), is slightly higher for BP LCO due to sharp overlapping regions between LCO grains. Roughness parameters based on surface and multi-line analysis are provided in Table S2. As already noted, similar texture control can also be achieved for electrodeposited NCO cathodes (see Supplementary Information 6).

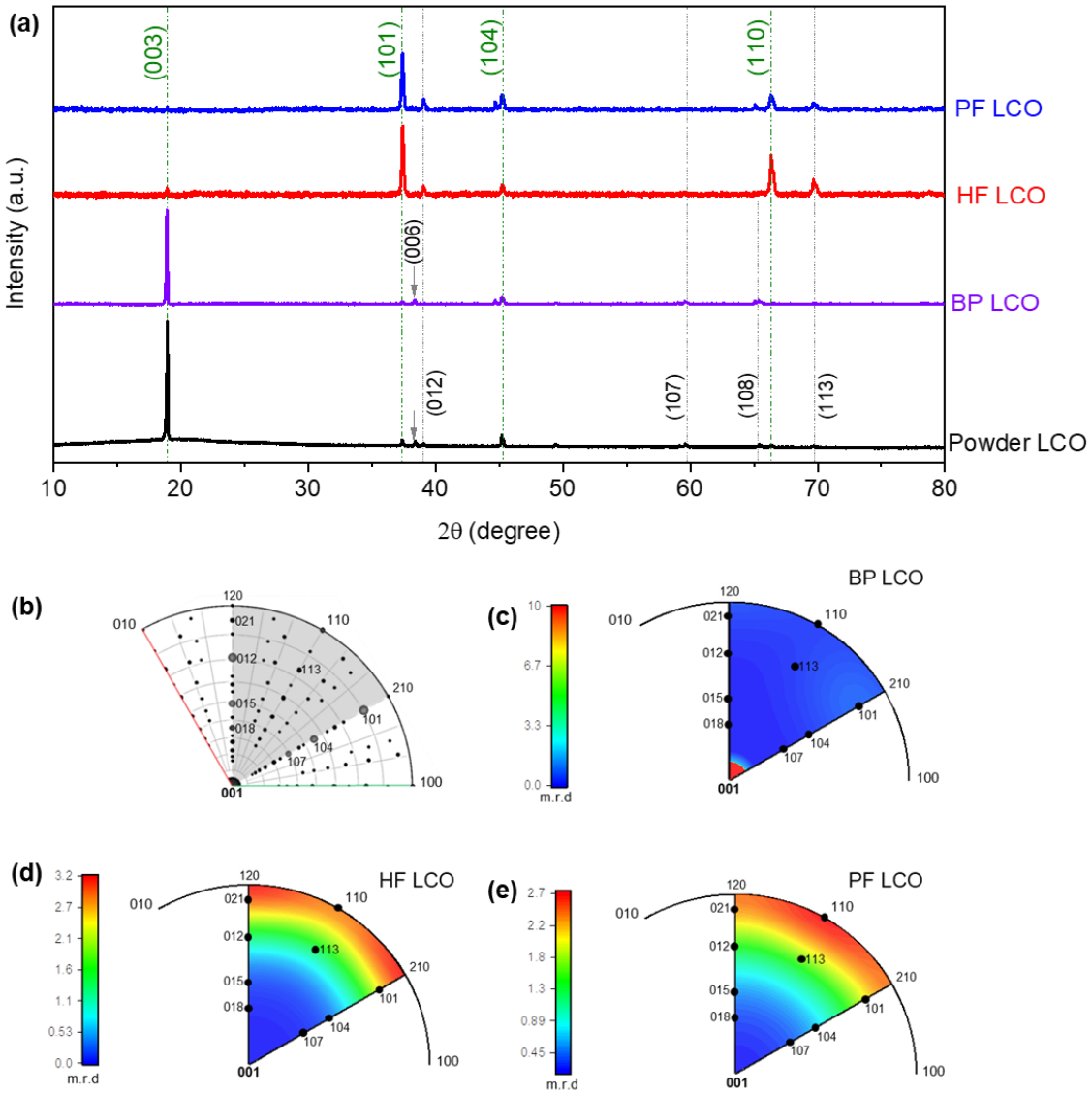

Figure S5. (a) X-ray diffraction patterns of as-plated dense LCOs and commercial LCO powder. (b) Reference stereographic projection of LCO crystal at [001] zone axis produced with WinWulff software (@JCrystalSoft). (c-e) Calculated inverse pole figures of dense LCOs in direction normal to the substrate (ND).

Table S1. Comparison of peak (areal) intensity ratio and texture coefficient (TC) of major planes for powder and electrodeposited LCO vs. standard LCO (PDF# 51182)

	$I_{003/101}$	$I_{003/104}$	$I_{003/110}$	$TC_{(003)}$	$TC_{(101)}$	$TC_{(104)}$	$TC_{(110)}$
LCO_{std}	5.24	1.53	5.89				
Powder LCO[#]	10.06	4.5	12.76	1.66	0.42	0.57	0.77
BP LCO	14.24	3.25	10.21	1.90	0.34	0.89	1.09
HF LCO	0.10	0.73	0.14	0.08	2.11	0.17	3.48
PF LCO	0.01	0.04	0.04	0.02	2.77	0.56	2.38

$TC_{(hkl)} = \frac{I_{(hkl)}/I_{0\,(hkl)}}{N^{-1}\sum_n I_{(hkl)}/I_{0\,(hkl)}}$ [3]

$I_{(hkl)}$: measure intensity of (*hkl*)

$I_{0\,(hkl)}$: standard intensity of (*hkl*)

N: number of reflections[*]

[*]Peaks for calculating TC: (003), (101), (104), (015), (107), (101)

[#]Powder LCO was measured in the as-received state

SI 5. Surface roughness analysis based on laser scanning confocal microscopy

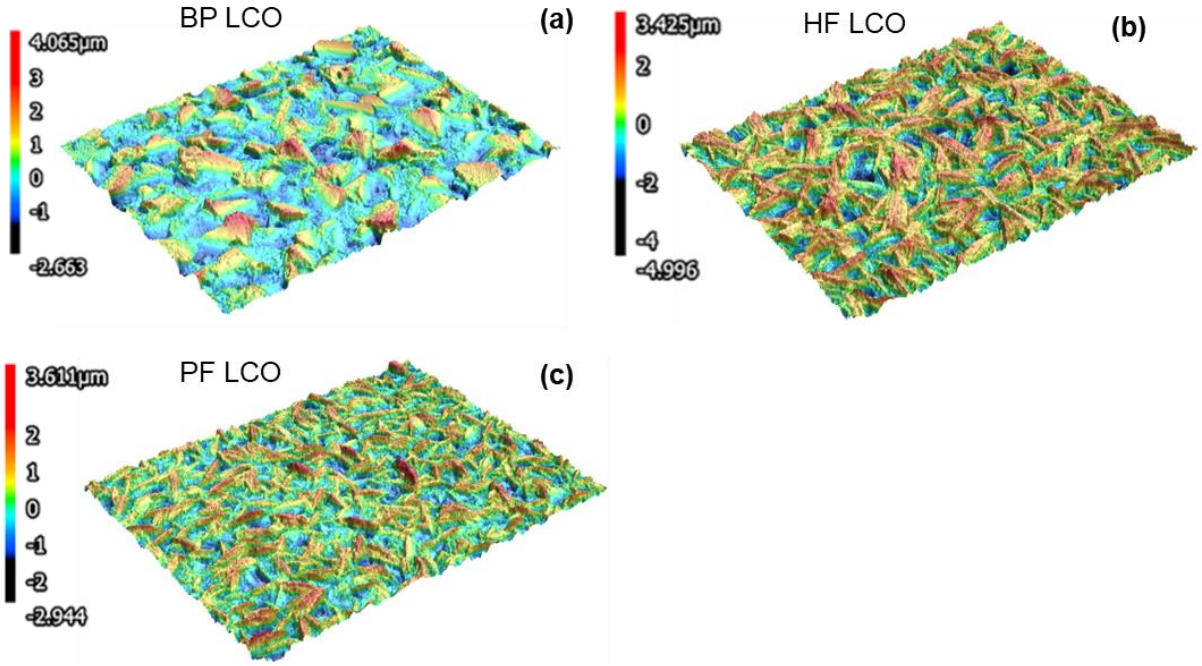

Figure S6. 3D surface profile of the (a) BP LCO, (b) HF LCO and (c) PF LCO. The colour bar shows the scaling of the colour profile to achieve optimal 3D graphic representation. All samples were measure with at the same area of 97×73 µm.

Table S2. Roughness parameters based on surface (S) and line (R) analysis

	Sa (µm)	Sq (µm)	Sz (µm)	Ra (µm)	Rq (µm)	Rz (µm)
BP LCO	0.709	0.886	8.421	0.732	0.907	4.902
HF LCO	0.543	0.687	6.555	0.530	0.663	3.718
PF LCO	0.649	0.818	6.728	0.691	0.866	4.641

Roughness definitions:

Sa, Ra (arithmetical mean height): average value of the absolute height at each point in the sampling area (S) or sampling length (R).

Sq, Rq (root mean square height): root mean square of height at each point in sampling area (S) or sampling length (R).

Sz, Rz (maximum height of the profile): sum of the maximum peak height and the maximum valley depth in sampling area (S) or sampling length (R).

SI 6. Dense sodium ($NaCoO_2$) cathodes

We also synthesized sodium cobalt oxide (NCO) with controlled orientation via. our electroplating route for the first time. The selection of NCO was based on its multiple-plateau charge-discharge characteristics due to strong tendency of Na^+-vacancy ordering of specific compositions[4] as well as high voltage properties (>4V vs. Na) which allows for examining the electrochemical stability range of halide SEs. Figure S7 shows the two distinct morphologies of plated NCO resembling that of LCO cathode, namely basal plane (BP) and highly faceted (HF) NCO. The preferred orientation of >10μm layers was confirmed by XRD analysis. Powder NCO (pNCO) was prepared by scraping and hand-grinding of similar plated NCO.

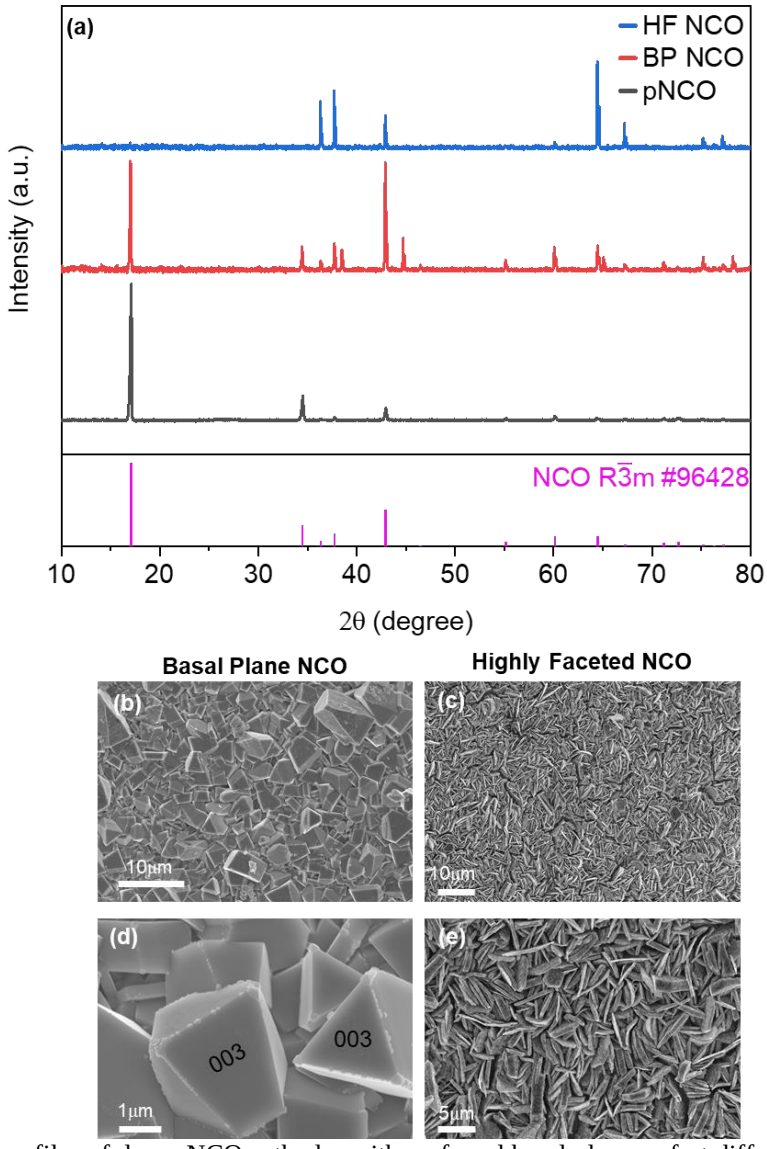

Figure S7. (a) XRD profiles of dense NCO cathodes with preferred basal plane or fast diffusing facet orientation as well as hand-ground powder. SEM image of top surface for (b,d) BP NCO and (c,e) HF NCO.

SI 7. Characterization of solid electrolytes

SI 7.1. Halide solid electrolytes for Li ion system

Two Li halide compounds were synthesized to study their compatibility and performance against dense LCO cathodes. Both Li_3YCl_6 (LYC) and Li_3InCl_6 (LIC) have shown high ionic conductivity and good electrochemical stability at high voltage[5,6]. We synthesized these compounds through intermittent high energy mechano-chemical (ball milling) route. Compared to conventional milling method, our approach features a significantly shortened processing time. The total processing time of LYC powder was 3-4 hours compared to 50 hours reported by Asano et al.[5]. The LIC powder was prepared by only one hour of high energy milling which is significantly lower than 24 hours reported by Li et al.[6]. Moreover, no further processing and post-treatment was conducted on the milling products. This is partly due to the adverse impact of heat treatment on the ionic transport properties of these two solid electrolytes. It was found that the ionic conductivity of highly crystalline LYC obtained by annealing at 550º C decreases by an order of magnitude[5]. This decrease was attributed to the loss of favourable Y^{3+} disorder within LYC structure. On the other hand, LIC was found to gain an almost two-fold conductivity after annealing at 250-400ºC [6]. Hence, LYC and LIC powders in as-milled state were used in this study. The crystal structure and ionic conductivity of the solid electrolytes are shown in Figure S8. The XRD profiles of LIC and LYC in Figure S8 (a) shows a typical low/nano crystalline nature similar to previous reports[5,6]. To ensure the proper phase was achieved, XRD profiles were also simulated based on the crystallography data available in the literature. For LIC, a monoclinic structure with $C2/m$ symmetry (ICSD No. 04-009-9027) was used. For LYC, the trigonal structure with $P\bar{3}m1$ space group reported by Asano et al.[5] was used. The ionic conductivity was measured using electrochemical impedance spectroscopy (EIS) and the corresponding Nyquist plots are shown in Figure S8 (b). Both halide structures show relatively high ionic conductivity without the presence of any grain boundary contribution based on the absence of any additional semi-circle. LIC powder shows slightly higher ionic conductivity (0.71×10^{-3} S cm^{-1}) compared to LYC powder (0.65×10^{-3} S cm^{-1}). These values are in well agreement with those reported for ball milled powders of these compounds in the literature[5,6].

The electrochemical stability of halide solid electrolytes was investigated by cyclic voltammetry (CV) test against a Li-In anode electrode. In a typical measurement, a SE pellet was sandwiched in between a Li-In anode/reference electrode and stainless steel cathode/current collector. The results of CV measurement and a cell assembly for such test are shown in Figure S9. It is worth noting that for the case of LIC, we used an extra layer of LYC (schematic in Figure S9) in the anode side to avoid redox reactions at the interface of LIC and Li-In[6,7]. The pellets were cycled between 1.9-4.0 V vs. Li-In (2.5-4.6 V vs. Li). The voltage window is narrower than that of a typical CV measurement on similar SEs in the literature[7,8]. This was intentional since the instability of these two electrolytes with respect to Li anode is well-established by theoretical and experimental work[5,7,9,10]. Moreover, from technical standpoint, the use of a narrow voltage window helps maintain the current reading of potentiostat instrument within the high accuracy range (see Methods). This allows us to detect any oxidation signal during the CV measurement. The inaccuracy of CV measurement in detecting the true stability of SEs due to suppression of oxidation peak by a large Li striping/plating peak pair has been pointed out by numerous authors[11,12]. Enhancement of electrochemical surface area by mixing the solid electrolyte with an inert conductive additive (ex. carbon or Pt powder) has been suggested as a tool to enhance the redox current reading[11,12]. However, it has been shown that carbon additives can induce unwanted oxidation reactions with some sulphide solid electrolytes[11]. Besides, adding even slightly varying amount of carbon additive to the SE powder may result in extremely different redox current magnitude and interfere with proper comparison between two electrolytes. Our CV results show a reasonable electrochemical current reading (well above the detection

limit). As can be seen in the CV plot, the LYC powder shows a small oxidation peak near 3.55 V vs. Li-In with some reversibility suggested by the reduction peak. On the hand, LIC oxidation starts at around 3.7 V vs. Li-In. These results clearly suggest better stability of LIC (by 0.2 V) compared to LYC. Both electrolytes show onset of some reduction near the lower band of voltage window. This could be due to the initiation of some reduction process which is more prominent in the case of LIC. Our impedance analysis and prior reports[5–7] affirm that the Li-In interface remains intact and is not the source of any instability. The onset of oxidation is most interesting to our analysis of SE stability at high LCO voltage. The observed oxidation potentials in our CV test are in agreement with the limited theoretical information available for these two compounds. According to Wang et al., LYC is expected to be stable up to 3.6 V vs. Li-In after which it decomposes to Cl_2 and YCl_3[10]. In contrast, LIC was predicted to be stable at voltages as high as 3.7 V vs. Li-In with $InCl_3$ and Cl_2 as the decomposition products[10]. Our results support these predictions although LYC shows slightly lower stability in our experiments compared to the predictions. Further confirmation of the lower stability of LYC compared to LIC is also presented via intra-cycle EIS measurements in SI 11.

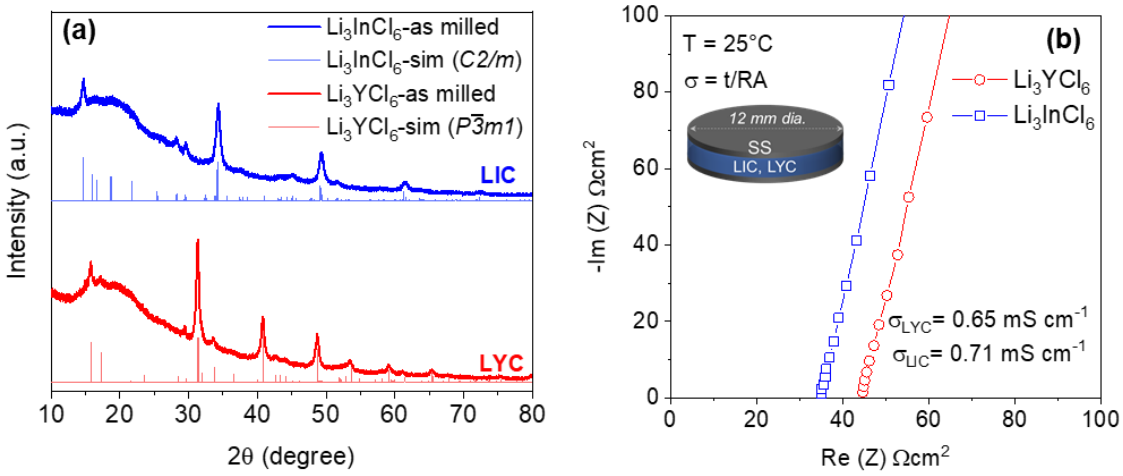

Figure S8. (a) X-ray diffraction of ball milled Li_3YCl_6 (bottom) and Li_3InCl_6 (top) powders. The line plots are simulated XRD pattern based on available crystallographic information for each compound. (b) EIS conductivity measurement of as-milled LYC and LIC powder sandwiched between two stainless steel plates under 360 MPa compression.

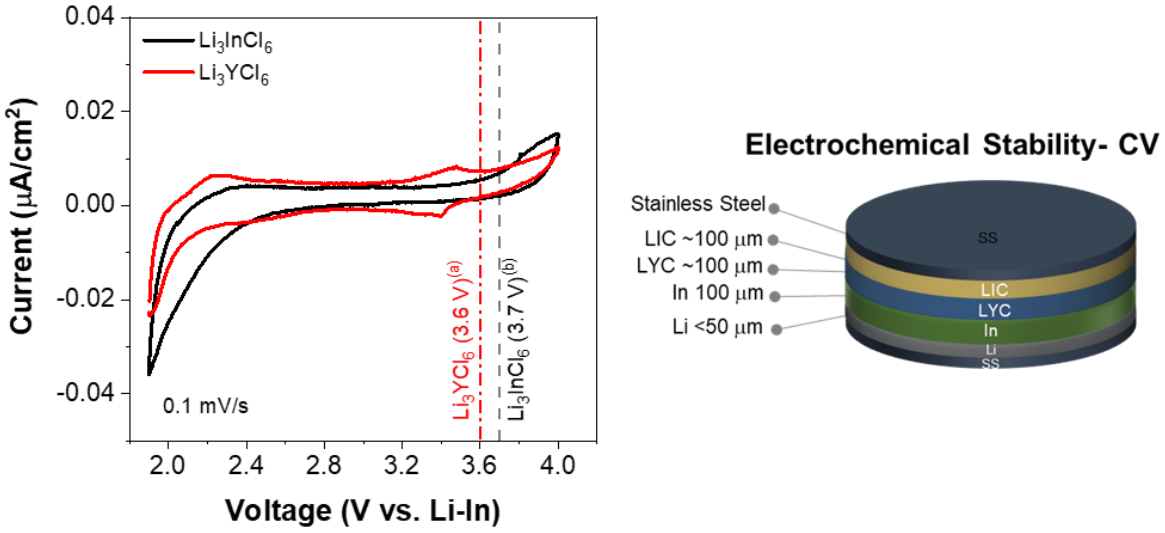

Figure S9. CV curves of the Li-In anode and stainless steel blocking electrode cells showing the electrochemical stability of Li_3InCl_6 and Li_3YCl_6 solid electrolytes. Predicted oxidation potentials (upper stability limit) of both electrolytes vs. Li-In (+0.6 V vs. Li/Li+) electrode are also shown. (a) and (b) are taken from Ref. [10]. Schematic construction of the cell for testing the LIC is shown one the right side. Note that the LYC is used near the anode to avoid the side reactions between LIC and In.

SI 7.2. Sulphide and halide solid electrolytes for Na ion system

In order to investigate the role of cathode crystallography on the cathode-SE interface stability, two types of Na conducting SE were explored. Na_3PS_4 (NPS) is the most common sulphide SE that has been vastly studied for solid-state Na ion batteries[13,14]. In its as-milled amorphous state, NPS suffers from poor ionic conductivity as confirmed by our EIS conductivity measurements in Figure S10. Although upon further milling, some gain in ionic conductivity is observed, the magnitude is far below practical range of 10^{-4} S cm^{-1}. Upon a short annealing period under Ar at 270 ºC, ball-milled NPS has been found to crystalize into a cubic phase (c-NPS) which shows a range of 0.4-2 × 10^{-4} S cm^{-1} ionic conductivity[13]. Further annealing beyond 270 ºC results in the formation of a tetragonal phase (t-NPS) with lower conductivity[13,14]. These findings are confirmed during our XRD characterization as shown in Figure S10. A new class of halide SEs inspired by the advent of their Li conductor counterparts has been recently reported. The new $Na_{(3-x)}Y_{(1-x)}Zr_xCl_6$ has been shown as a stable SE against $NaCrO_2$ cathode owing to the SE's high oxidation stability of 3.8 V vs. Na (3.6 V vs Na-Sn)[15]. As the most conductive member of series, $Na_{2.25}Y_{0.25}Zr_{0.75}Cl_6$ (NYZC75 or NYZC in this manuscript) was fabricated via solid-state mechanical route. The crystal structure resembles that of reported in Ref. [15] while ionic conductivity lies in the lower end of reported range. Our attempt at other compositions also yielded a similar conductivity suggesting the prolonged high temperature post-treatment at 500 ºC is essential to obtaining the 6.6 ×10^{-5} S cm^{-1} reported value[15]. While achieving higher ionic conductivities are desirable for cell cycling performance, the obtained value from ball-milled powder serves as suitable proxy for a halide Na-ion conducting SE family.

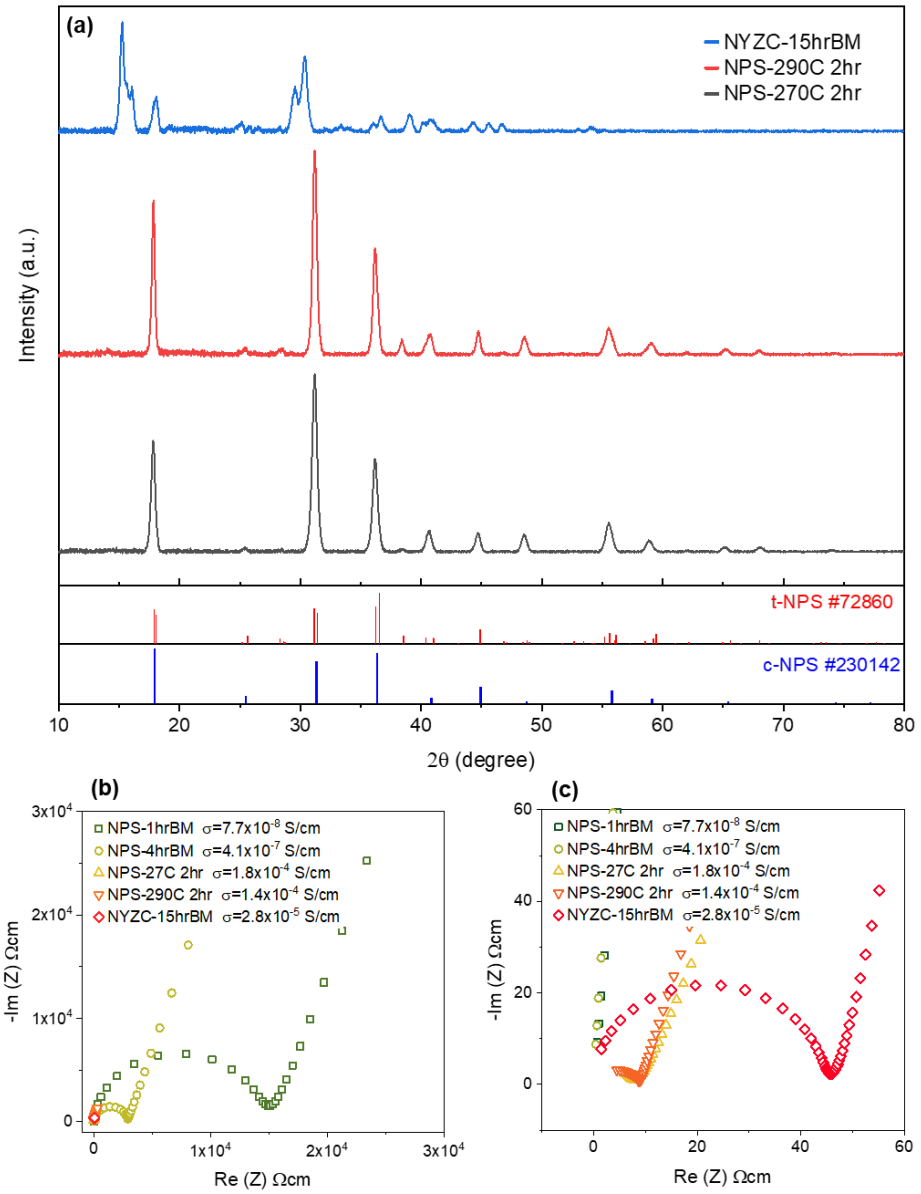

Figure S10. (a) XRD analysis of annealed NPS at 270 and 290 C as well as ball milled NYZC powder after 15 hours of milling. (b and c) EIS ionic conductivity measurement of NPS before and after annealing showing significant role of cubic NPS phase. Ionic conductivity values of all samples are listed in the inset.

SI 8. Liquid cell performance of dense LCOs

Conventional LIB tests (Figure S11) also showed dense LCOs possess good electrochemical performance similar to high quality electroplated LCOs[16]. BP LCO showed unexpectedly higher initial coulombic efficiency (ICE) compared to faceted LCOs. Studies of thin film LCOs with specific surface texture have shown lowest ICE for (003)-textured films[17]. We speculate that the "free space" in between large BP LCO grains (Figure S2 (a,b)), easily accessible to the liquid electrolyte, diminishes the texture effect. The low ICE value of PF LCO can be due to extra 20 mV discharge overpotential based on dQ/dV

plots Figure S11 (d-f). The sharp peak near 3.9 V vs. Li corresponds to the well-known first-order phase transition of insulating to metallic Li_xCoO_2 ($0.75<x<0.93$)[18]. The peaks near 4.05 and 4.15 V vs. Li correspond to the order-disorder phase transition between rhombohedral and monoclinic structures[18]. These phase transitions are identified by H>M and M>H on these plots where H stands for hexagonal (rhombohedral) and M denotes monoclinic. The observation of order-disorder transition has been associated with the high purity of LCO and proposed as a measure of quality[19]. Cycling performance of the cells at 0.2C, in Figure S11 (g), also confirms fairly similar stability among dense LCOs, making them suitable for understanding interfacial properties using high voltage halide solid electrolytes.

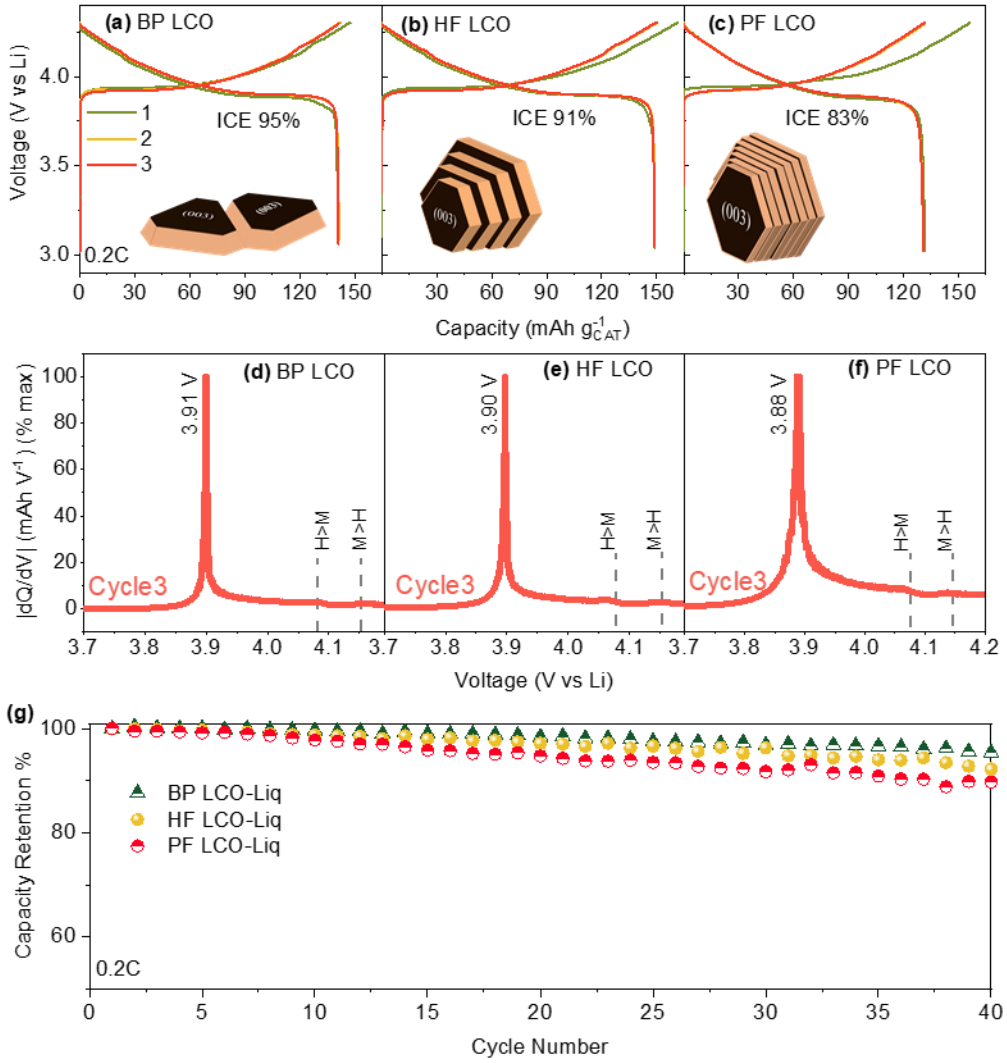

Figure S11. Charge-discharge curves of electroplated LCOs in conventional liquid battery testing. (a) shows the initial three cycles at 0.2 C rate. (b) absolute values of dq/dV based on third discharge half cycle shows slightly higher overpotential for PF LCO. Dashed lines correspond to the known phase transition in $LiCoO_2$ during dis/charge. Note: the plots are extracted from the discharge curves and the position of each peak corresponding to a certain polarization should be taken with reference to the highest voltage point. (c) cycling performance of dense LCOs at 0.2 C for first 40 cycles shows similar stability.

SI 9. Solid-state cell performance

SI 9.1. Dense LCOs vs. composite cathodes

Electroplated LCOs were tested for their structural and chemical stability in a solid-state cell configuration. Figure S12 (a) shows that typical 360 MPa pressure for fabrications of conventional composite cathode, is also needed for dense LCOs to avoid losses due to contact resistance. Thermal stability of LCO-halide SE under high compressive force, examined by XRD analysis (Figure S12 (b)), also proves chemical stability at elevated temperatures.

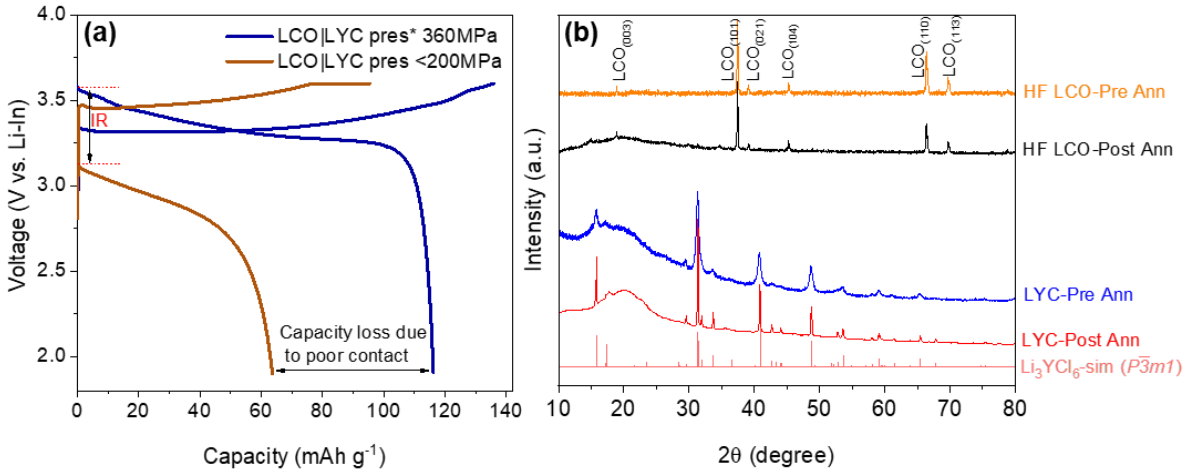

Figure S12. (a) First charge-discharge curves of two LCO|LYC pellets made at different compression showing the IR losses due to the poor contact between the cathode and solid electrolyte. The cell structure is cathode|Li_3YCl_6|Li-In cell in both cases. Asterisk refers to the compression pressure. (b) XRD profile of HF LCO-LYC compressed pellet after annealing at 300º C (12 h) compared with pre-annealing state showing no reaction/instability.

Figure S13 (a-h) show the charge-discharge curves of dense and composite LCOs using LYC and LIC in the first three cycles at 0.1C rate. Note that the capacity is reported on the basis of total cathode weight (mAh g_{CAT}^{-1}) accounting for weight of SE in composite cathode. The specific capacity of composite cathodes based on active material still remains in the vicinity of theoretical 140 mAh g^{-1}, confirming full utilization of LCO powder. Composite cathodes display relatively high ICE value of 91% in agreement with previously reported findings[5,6]. In the case of dense cathode, ICE seems to be strongly dependent on LCO texture/morphology with BP LCO having the lowest coulombic efficiency and HF LCO displaying ICE values on par with composite cathodes. Dense LCO-LIC systems show improved ICE and slightly better initial stability. Overall, there exists a clear variation in ICE values of composite vs. dense cathode as well as amongst various dense cathode texture and morphologies. However, the ICE values of HF-LCO and composite cathodes are roughly in the same range. As corroborated by our intra-cycle impedance (Figure 4 in main manuscript) data and reported GITT (SI 10) results, the overpotential caused by solid electrolyte, specifically LYC, oxidation near the end of full charge, as well as crystallography of cathode, BP LCO vs. HF LCO, and morphology of cathode, PF LCO vs. HF LCO, all contribute to such variation in the ICE value. Moreover, the large interfacial area of a composite cathode can also prevent the observation of any interfacial instability and the resulting impact within the first cycle.

Analysis of dis/charge curves by dq/dV plots (Figure S15) shows that all samples display the first-order transition peak near 3.3 V vs. Li-In (3.9 vs. Li). Broadening of this peak in BP LCO samples corresponds to a sloped plateau in the discharge curve and is most likely due to sluggish phase transition kinetics and higher polarization. This can also explain lower ICE value of BP LCO. The peaks near 3.45 V and 3.55 V vs. Li-In corresponding to monoclinic-hexagonal transition are also present. Position of large first-order transition peak is ~10 mV lower for cLCO compared to all dense LCOs suggesting higher discharge overpotential. Moreover, the dq/dV plots suggest poor performance when LYC is used with dense LCOs which is most likely due its lower oxidation stability in CV measurement. The M>H transition in BP LCO (peak at 3.55 V vs. Li-In) seems either absent or negligible. This was confirmed by XRD refinement analysis (Figure S15-17) where BP LCO shows a single monoclinic phase in charged state. On the other hand, HF and PF LCO show mixture of monoclinic and hexagonal phases in line with the appearance of M>H peak in their dq/dV profiles. The lack of sufficient ionic pathways at the surface of BP LCO, and hence, sluggish kinetics, is most likely the underlying reason for the incomplete phase transition. Many studies have linked the monoclinic transition to long-term capacity fading of composite cathodes and proposed doping or surface coating routes toward its suppression[20,21]. A survey of recent studies shows that the LCO phase transition behaviour has not been fully understood in LCO-halide solid electrolyte systems. For instance, the dis/charge curves of cLCO-LYC and cLCO-LY(Zr)C show negligible sign of monoclinic phase transition[5,22]. On the other hand, cLCO-LIC reported by Li et al.[6] demonstrates a distinct monoclinic transition in both dis/charge curves and CV measurements. Coincidentally, the latter study shows more capacity fading during cycling compared to those reported with LYC and LY(Zr)C solid electrolytes. We believe the impact of this phase transition on the properties of solid-state cells is a critical subject matter which has been somewhat overlooked in most recent studies.

Cycling results in Figure S13(i) and S14 also shows a clear outperformance of LIC over LYC especially for dense LCOs. Composite cLCO-LIC shows similar capacity retention to prior reports[6]. However, cLCO-LYC is less stable than similar composite reported previously[5] most likely due to different cycling rate and absence of clear order-disorder phase transition in that study. The poor performance of LYC becomes even more pronounced when used with dense LCOs (Figure S13(i) middle row). A low capacity retention of ~55% was observed for all electroplated cathodes. Since all dense LCOs show similar phase transition behaviour, we hypothesize the poor performance of LYC may solely arise from the oxidation of LYC at the interface (see Cathode-SE Interface Transport Properties section of the main text). In contrast, dense LCO-LIC show excellent cycling performance. The HF and PF LCOs show high capacity retention of 88% after 70 cycles. Capacity retention of BP LCO remains in the vicinity of 71% at the end of cycling pointing out the lack of sufficient Li de/intercalation pathways at the surface. Combining the findings of our CV measurement on SE stability (Figure S9) and cycling data, we conclude that the performance of SSBs may be adversely impacted by even 0.2 V difference in interfacial electrochemical stability. The severity of impact becomes exaggerated when the cathode-SE interface is significantly reduced to only a top surface as with the case of dense LCO. In other words, the interfacial instability issues due to oxidation might remain unnoticed when composite powder mixture are investigated.

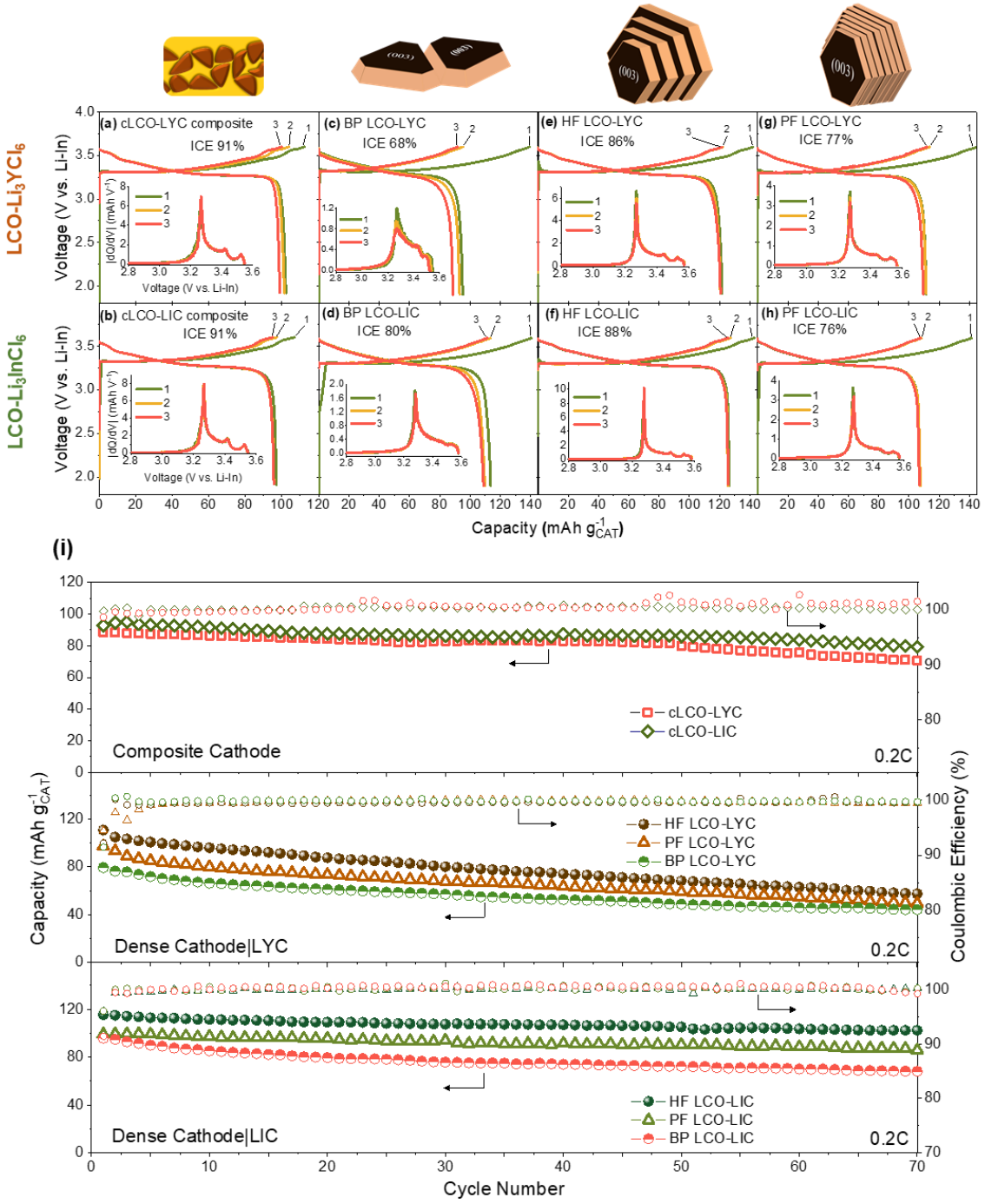

Figure S13. Charge-discharge curves of the initial 3 cycles (0.1C) for (a,b) powder LCO, (c,d) BP LCO, (e,f) HF LCO and (g,h) PF LCO using LYC (top row) and LIC (bottom tow) as solid electrolyte. Insets show discharge |dq/dV| curves for the first 3 cycles. Initial coulombic efficiency (ICE) is also reported on each graph. (i) Cycling performance (0.2C rate) of SSBs for composite cathode-SE mixture (top row), dense LCO-LYC (mid row) and dense LCO-LIC (bottom row). Note: capacity is reported based on total cathode weight. Composite (cLCO) cathodes contain 20 wt.% of non-active SE.

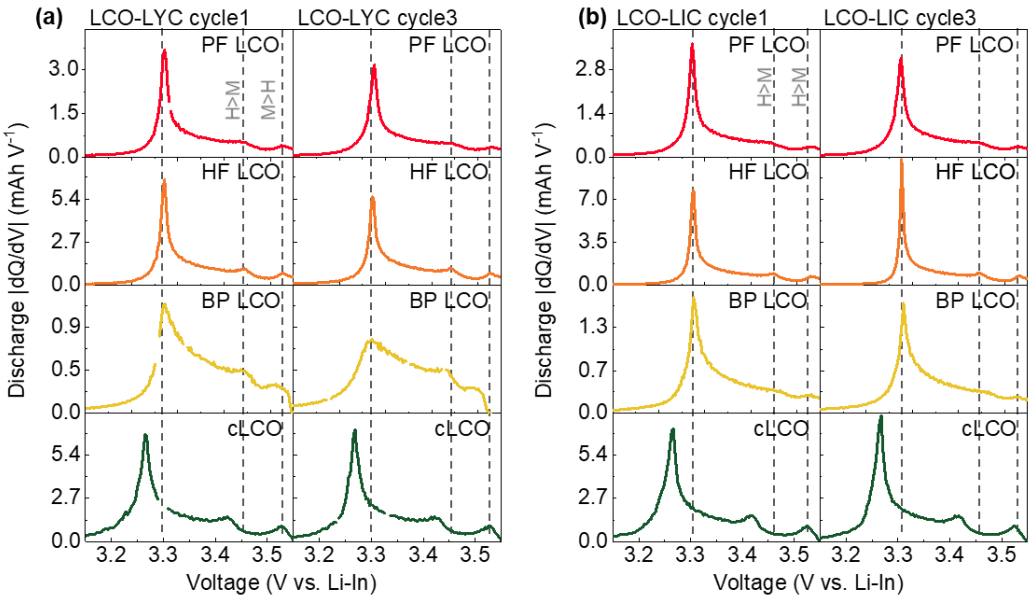

Figure S14. Absolute values of dq/dV based on the first three discharge half cycles (0.1C) for solid state cells made with (a) LYC and (b) LIC solid electrolytes. Dashed lines correspond to the known phase transition in $LiCoO_2$ during dis/charge. Note: the plots are extracted from the discharge curves and the position of each peak corresponding to a certain polarization should be taken with reference to the highest voltage point.

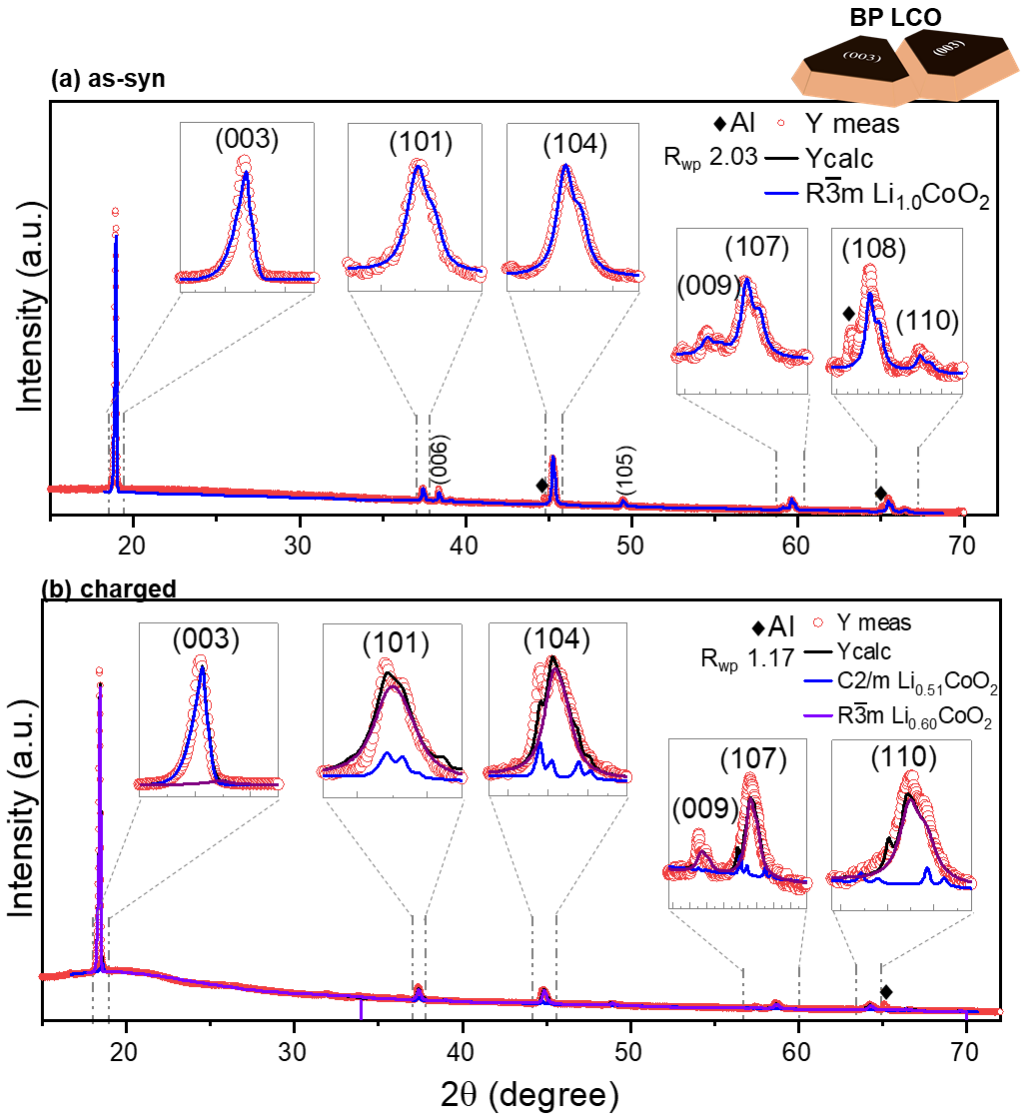

Figure S15. XRD analysis of BP LCO structure in the (a) as-synthesized and (b) charged ($Li_{0.5}CoO_2$) state.

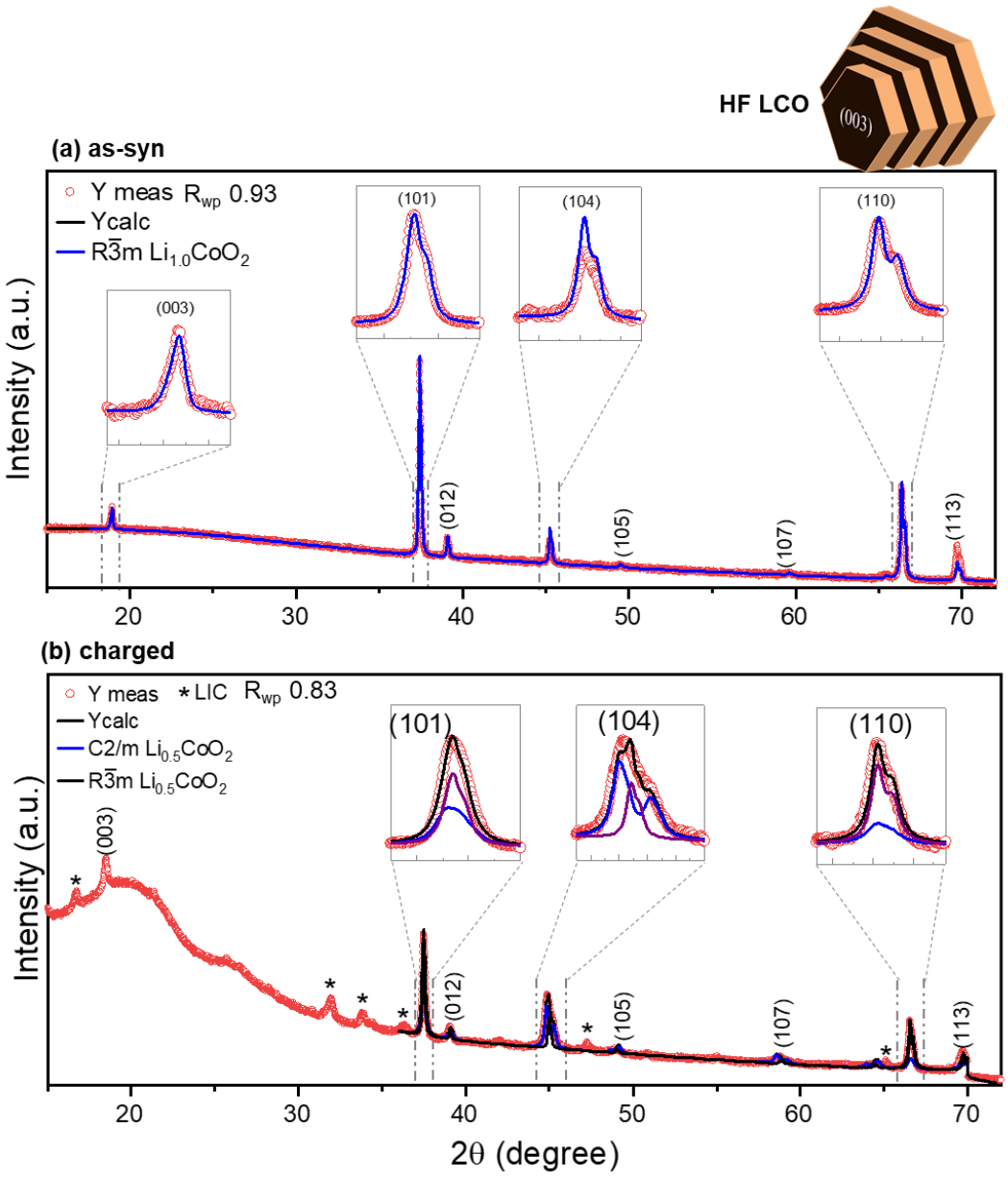

Figure S16. XRD analysis of HF LCO structure in the (a) as-synthesized and (b) charged ($Li_{0.5}CoO_2$) state.

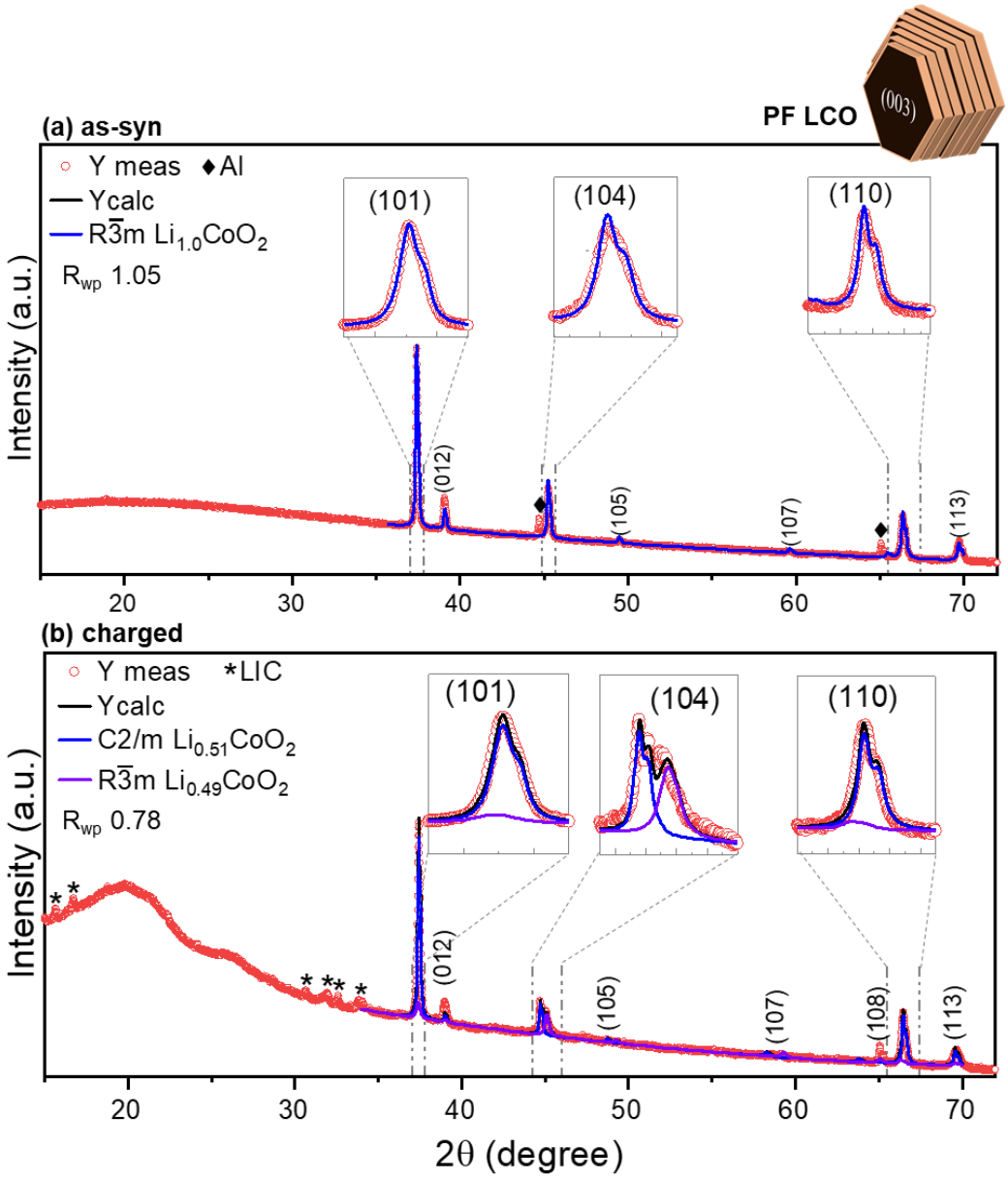

Figure S17. XRD analysis of PF LCO structure in the (a) as-synthesized and (b) charged ($Li_{0.5}CoO_2$) state.

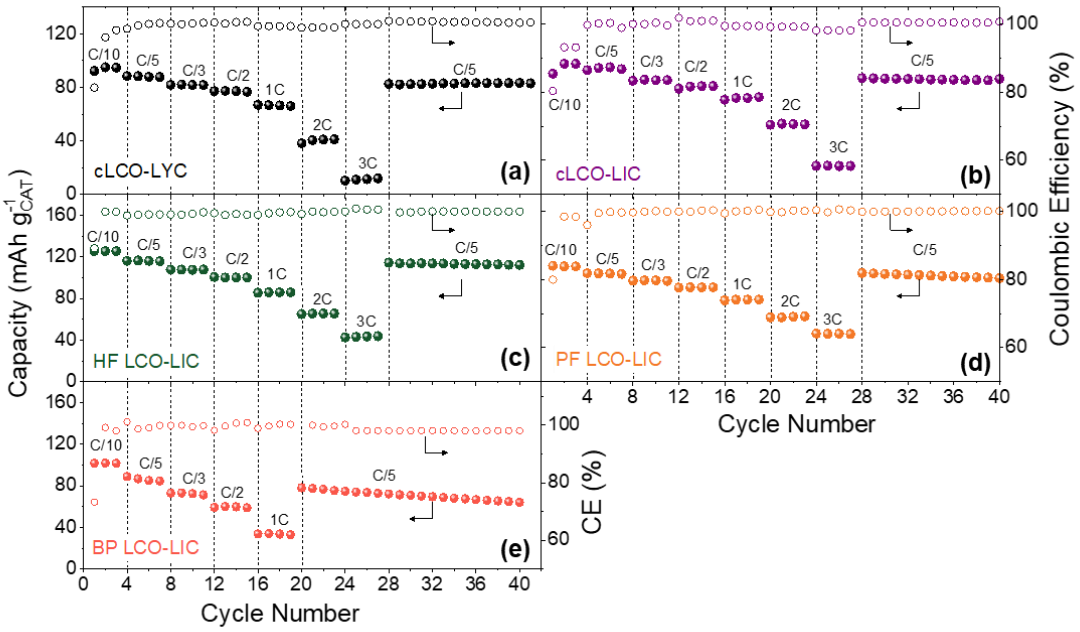

Figure S18. Rate capability measurements using same charge-discharge for (a,b) powder LCO-SE mixtures and (c-e) dense LCO-LIC solid state cells.

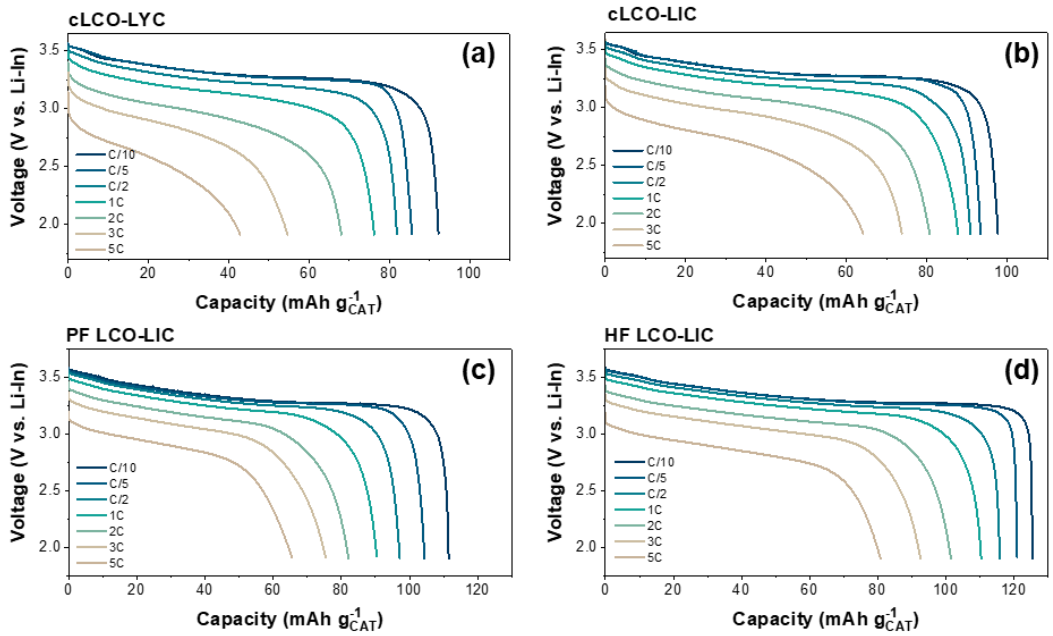

Figure S19. Discharge retention capability using slow 0.1 C charge rate for (a,b) powder LCO-SE mixtures and (c,d) dense LCO-LIC solid state cells.

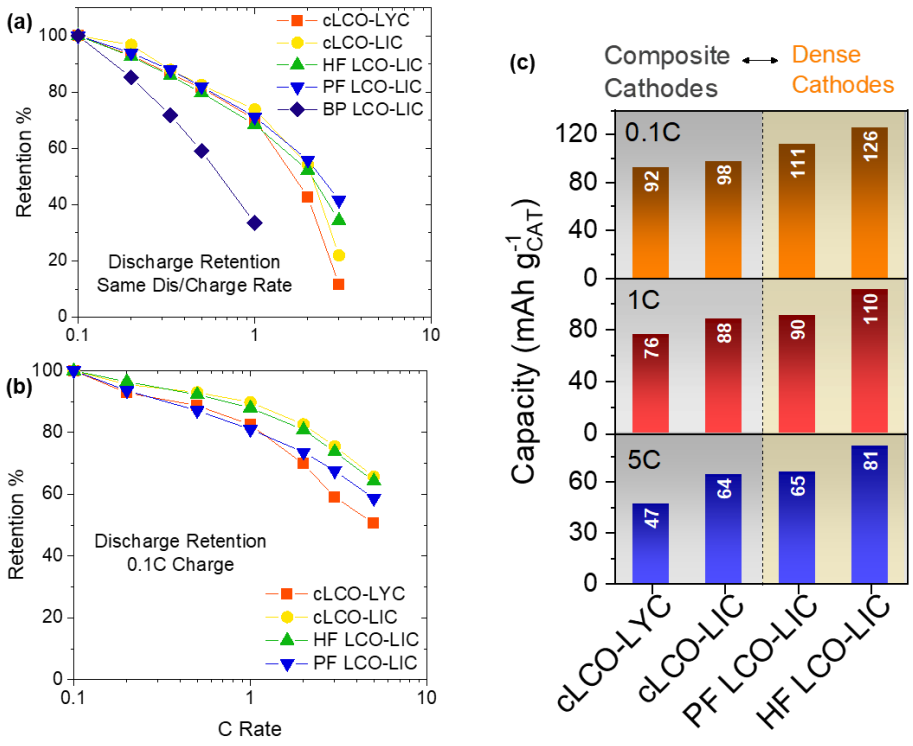

Figure S20. (a, b) Summary of rate performance data obtained based on two testing protocols. (c) Total discharge capacity (charged at 0.1C) at 0.1C, 1C, and 5C discharge for composite cathodes using both LYC and LIC SE (left) and PF and HF LCOs interfaced with LIC (right). Note: Dense LCO-LYC systems are excluded from rate performance tests due to poor cycling performance.

SI 9.1.1. Thick LCO SSB testing

The areal capacity of thicker electroplated LCO in the highly faceted texture in the form of discharge capacity retention performance measurement is shown in Figure S21. As can be seen in this plot, the LCO|LIC|LYC|In cell can deliver around 2 mAh cm^{-2} with about 0.7 mA cm^{-2} current density and about 1.5 mAh cm^{-2} using a high current density of 1.8 mA cm^{-2}.

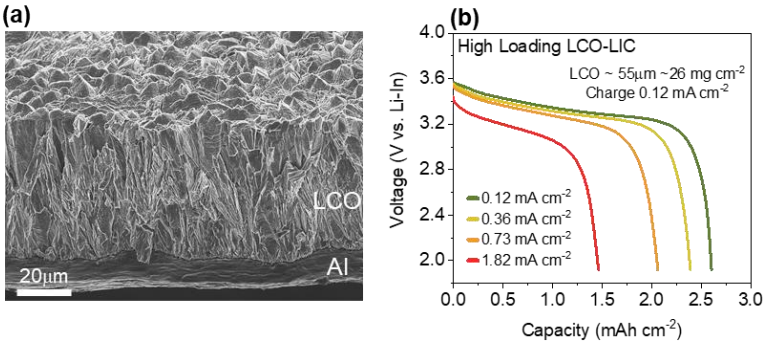

Figure S21. (a) SEM cross section of a thick HF LCO layer on Al foil with a nominal thickness of 55 µm. (b) shows the discharge areal capacity of 55 µm thick-LCO in LCO|LIC|LYC|In solid-state cell at different current densities.

SI 9.1.2. Impact of LCO loading and cycling rate

Limited testing on two different thicknesses of electroplated HF LCOs was performed and shown in Figure S22. We note that we intentionally opted for 10 µm and above thickness for LCO since thinner samples do not provide technically relevant loadings. During our 0.5C testing, we did not see a significant variation in stability over 50 cycles as Figure S22(a) shows. We also highlight our cycling data comparison of cycling performance of HF LCO-LIC at different rates does not yield a clear trend of variation over rate as Figure S22(b) shows.

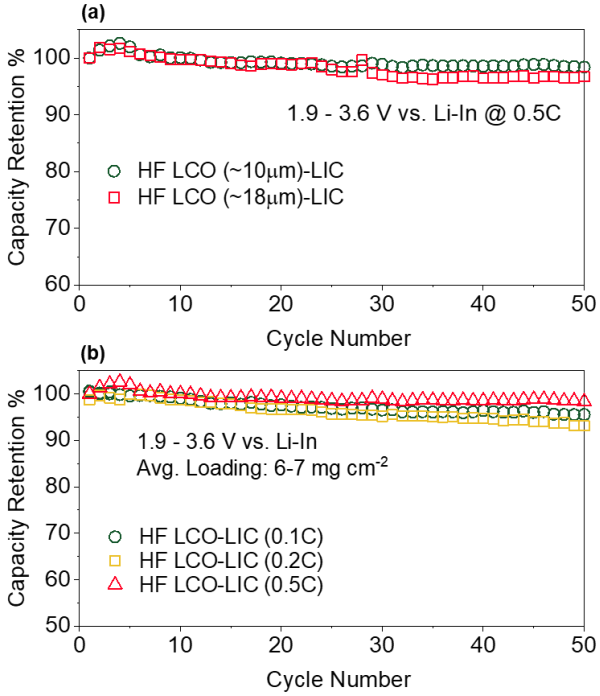

Figure S22. (a) Variation of cycling stability with respect to cathode loading explored in HF LCO-LIC systems during cycling at 0.5C rate. (b) Comparison plot of cycling stability of the 10µm HF LCO with LIC solid electrolyte at three different C rates.

SI 9.2. Dense NCOs vs. composite cathodes

The charge-discharge properties of NCO cathodes were examined in NCO|NYZC|NPS|Na-Sn solid state cells. The use of Na-Sn (0.2 V vs. Na) is due to avoid instability issues of NPS against pure Na anode. Moreover, NPS serves as a buffer to account for the instability of NYZC SE below 1.5V vs. Na due to the thermodynamic reduction of Zr^{4+} ions[23]. Figure S23(a) demonstrates the initial charge-discharge curves of composite and dense NCO cathodes with NYZC as the SE. all tests were performed at a 0.1C rate. Charging O3 $NaCoO_2$ in the 2.0-4.0 V (vs. Na) voltage range corresponds a desodiation of 0.59 moles of Na out of which 0.42 moles can be reintercalated back into the structure due to the first cycle irreversible formation of O'3 from O3[24]. The structure becomes electrochemically reversible after conversion of the O'3 to P'3 resulting in a highly reversible capacity of about 60 mAh g^{-1} according to our liquid cell data and prior literature[24]. Beside inherent low ionic conductivity of NYZC, a possible oxidation of SE during the last stage of charge from 3.6 to 3.8 V vs. Na-Sn, can also be responsible for a higher overpotential effect. The choice of 3.8 V vs. Na-Sn (4 V vs Na) is to examine the degree of SE oxidation with respect to cathode morphology and crystallography and its impact on interfacial stability throughout cycling. As can been seen in Figure S23(b), the HF NCO shows the highest capacity stability while composite cathode

shows most capacity fading over the 30 cycle. It is evident that the extent of oxidation is most severe in the composite cathode where extensive oxidation can occur in the interface.

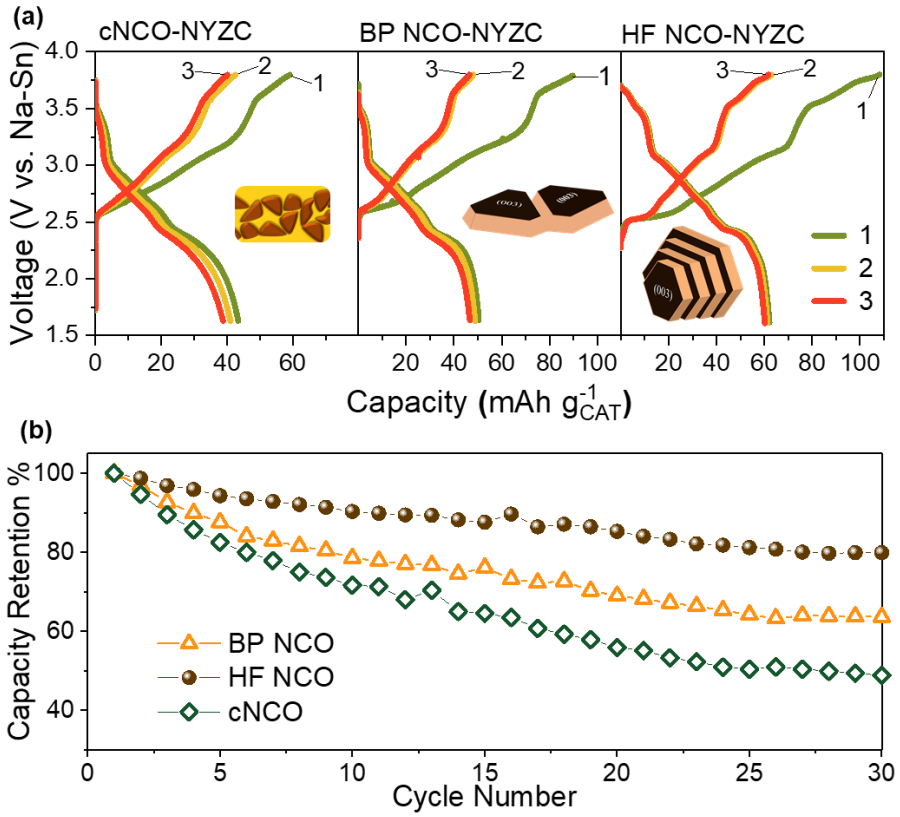

Figure S23. Charge-discharge curves of the initial 3 cycles (0.1C) for composite NCO, BP NCO, HF NCO using NYZC as solid electrolyte. Cell structure consists of an NPS layer near Na-Sn anode. Note: capacity is reported based on total cathode weight. Composite (cNCO) cathode contain 35 wt.% of non-active SE. (b) Cycling performance (0.1C rate) of SSBs for all systems in form of capacity retention percentage.

SI 10. GITT analysis

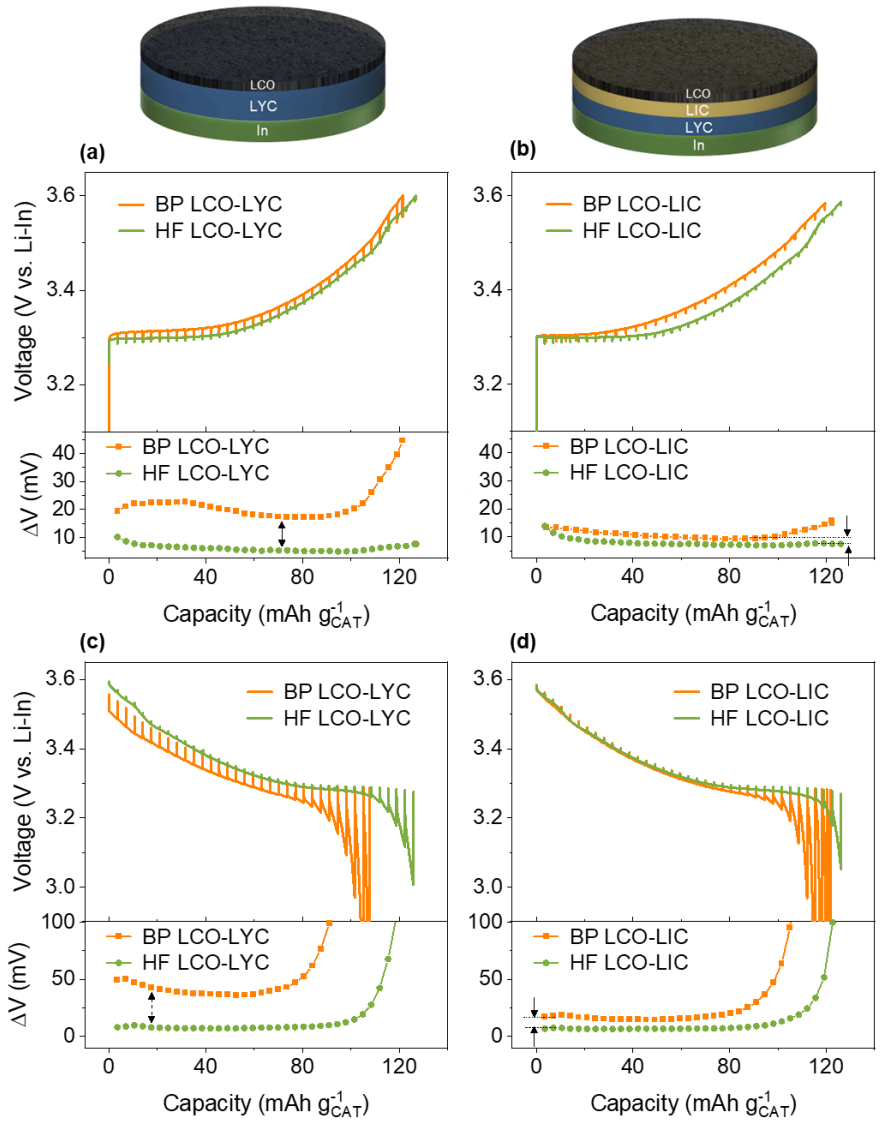

Figure S24. GITT test of HF LCO and BP LCO with LYC (left) and LIC (right) solid electrolyte under 0.05 C pulse and 1 hour rest condition. (a) and (c) show the charge and discharge GITT results for LCO with LYC. (b) and (d) show the charge and discharge GITT results for LCO with LIC. The bottom charts show the overpotential measured after each pulse step. Note: overpotential values are plotted with similar y-axis scaling to emphasize the impact electrolyte and crystallography.

SI 11. EIS analysis

SI 11.1. Li-ion systems

SI 11.1.1. Intra-cycle EIS

Figure S25 shows an example of an intra-cycle measurement for the first charge-discharge cycle in a HF LCO|LYC|Li-In cell measured in 10 steps. We used two different models in our analysis of EIS data as

shown in Figure S26. The main difference between the two models is how the information at high frequency (HF) region (>10kHz) is treated. It is well-stablished that the semi-circle at HF region (R_2Q_1 in 3RQ model) corresponds to extremely fast process such as SE ionic conductivity (R_{Li+} in Figure S26 (b))[25,26]. The resistance value extracted from this region does not vary over cycling in our study which is in line with prior reports[26,27]. Moreover, throughout our study, we have found the semi-circle in HF region can become combined with the neighbouring semi-circle suggesting a proximity of time constant values of the underlying processes making its deconvolution rather impossible. The semi-circle at low frequency (LF) region (<10 Hz) with a typical characteristic frequency of 1 Hz and capacitance in mF range has been correlated with Li concentration in Li-In alloy anode (R_a) [28,29]. The inclined tail toward the very low frequencies (<100 mHz) corresponds to slow mass-transport (Li^+ diffusion in LCO) related processes. The most important portion of EIS profile in our study, the mid frequency (MF) region (10 kHz – 10 Hz) and μF capacitance range, has been found to correspond to charge transfer through cathode-SE interface[5,6,28–30]. In fact, the MF region is the only feature of EIS profile that shows variation during intra- and inter-cycling measurements. Considering the bulk ionic transport properties of SE pellet (HF region) are invariant with respect to voltage and cycling, we attribute any change in the MD region to interfacial transport properties. Hence, the resistive element in the RQ pair from MF region provides the key parameter $R_{LCO|SE}$. The particular frequency range of this region allows to use either 2(RQ) (especially when overlapping time constants are present) or 3(RQ) equivalent circuit models and obtain similar interfacial resistance values as shown in the summary Tables in Figure S26.

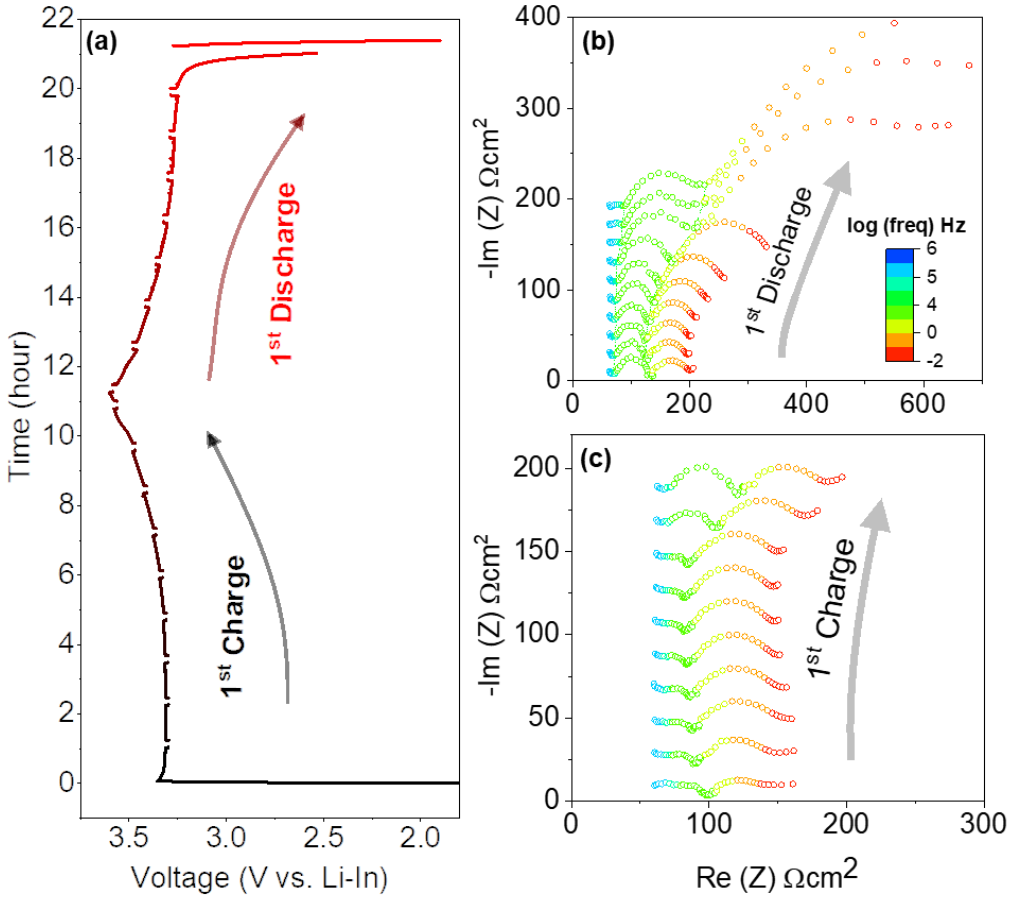

Figure S25. Intra-cycle impedance measurement during the initial charge-discharge cycle for the HF LCO|Li_3YCl_6|LiIn cell. EIS data points are coloured based on their corresponding frequency as shown in the inset colour map in (b).

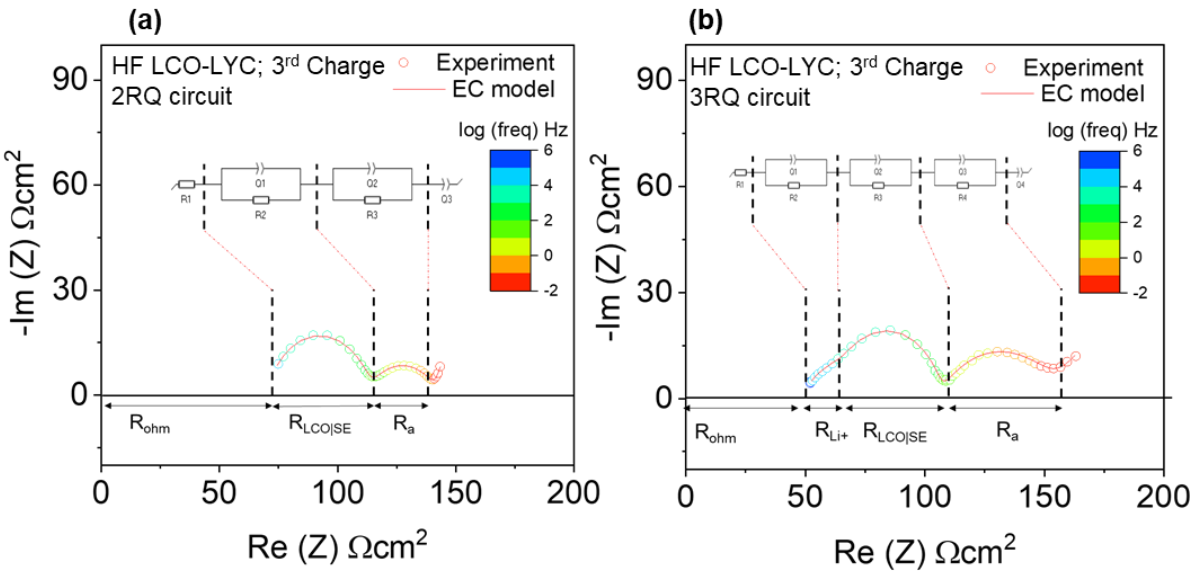

Resistance	Ωcm²	Capacitance	Fcm⁻²
R_{ohm}	70.07		
$R_{LCO\|SE}$	43.52	$Cap_{LCO\|SE}$	2.06×10^{-6}
R_a	27.72	Cap_a	1.96×10^{-3}

Resistance	Ωcm²	Capacitance	Fcm⁻²
R_{ohm}	51.30		
R_{Li+}	10.77	Cap_{Li+}	5.11×10^{-7}
$R_{LCO\|SE}$	43. 83	$Cap_{LCO\|SE}$	2.55×10^{-6}
R_a	47.74	Cap_a	4.80×10^{-3}

Figure S26. Examples of equivalent circuits (ECs) based on (a) 2 and (b) 3 RQ circuits accommodating for different components of the measured EIS Nyquist plot. Both plots correspond to measurement at the 3rd charged state of two similar HF LCO|Li_3YCl_6|Li-In cells collected with two separate instruments. (a) corresponds to a low (10 kHz) and (b) corresponds to high (1 MHz) frequency instrument range. Tables summarize the magnitude of resistive components based on each model showing similar interfacial resistance regardless of the model. R_{ohm}, $R_{LCO|SE}$, and R_a correspond to cell ohmic resistance, LCO|SE interfacial resistance and Li-In anode resistance, respectively. Note: R_{ohm} in (a) corresponds to sum of ohmic and SE conductivity which cannot be resolved due to lack of high frequency data.

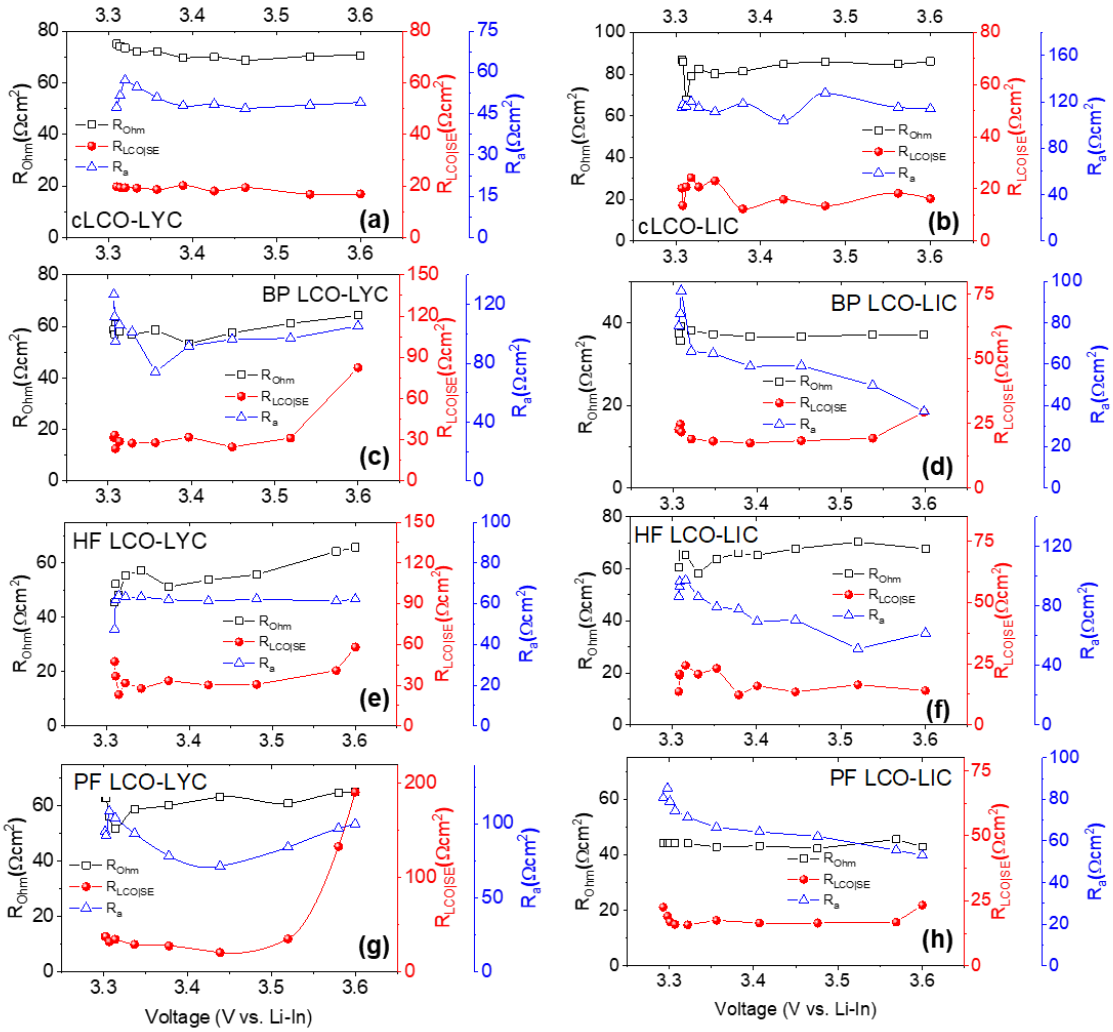

Figure S27. The evolution of different resistance components during the first charge cycle of (a) composite $LiCoO_2$-Li_3YCl_6 composite, (b) BP, (c) HF and (d) PF LCOs in the cathode|Li_3YCl_6|Li-In cells.

SI 11.1.2. SE electrochemical stability via EIS intra-cycle test: LYC vs. LIC

To showcase the use of dense cathodes and intra-cycle impedance tracking in identifying oxidation stability, we performed a test where a BP LCO-LIC SE was charged to even higher voltages beyond 3.6 V vs. Li-In (4.2 V vs. Li). As the plot in Figure S28 shows, further charging of a dense LCO-LIC cell causes oxidation of the SE judging by the increase in interfacial resistance. We believe this observation further demonstrates that using a dense cathode and tracking the impedance at the cathode-SE interface provides a more realistic picture of SE oxidation stability during the operation of solid-state cells.

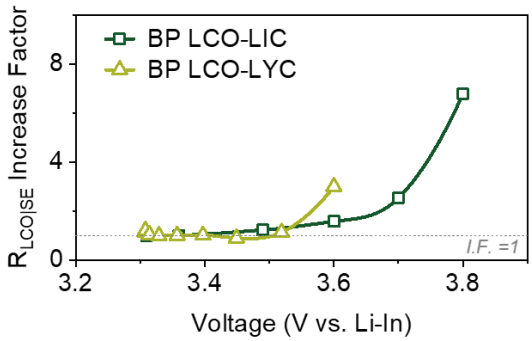

Figure S28. Comparison of increase in interfacial resistance for a BP LCO against LYC and LIC solid electrolytes. The interfacial resistance is reported as a relative value for easier comparison. I.F. stands for "increase factor" on the chart. The cell assembly is LCO|LYC|In and LCO|LIC|LYC|In for the case of LCO-LYC and LCO-LIC, respectively. Cell pressure of 70-80 MPa and LCO loading of 6-7 mg cm^{-2} was used.

SI 11.1.3. Inter-cycling EIS tests: 0.2C cycling

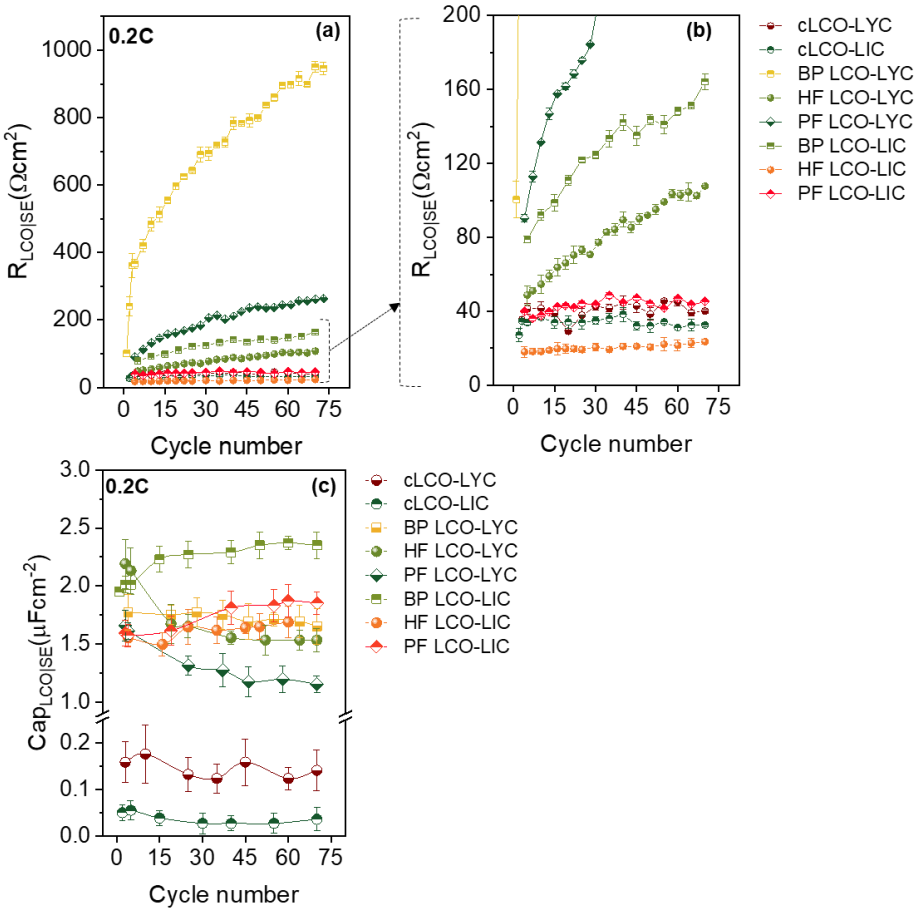

Figure S29. (a,b) Interfacial resistance and (c) effective interfacial capacitance at fully charge state for composite and dense LCO-halide solid electrolyte systems during cycling at relatively slow rate of 0.2C rate. Error bars are produced on the basis of three consecutive EIS scans and error analysis of effective capacitance extracted from CPE parameter.

SI 11.1.4. Inter-cycling EIS tests: 0.1C cycling

Figure S30 shows the cycling data for LCO-LYC systems at 0.1C. As the graph of capacity fade vs. interfacial resistance shows, there still exists a consistent linear relationship which is non-existent in composite system. These results suggest that the oxidation of LYC at the LCO interface still occurs even at lower current densities with a similar rate than that of 0.2C cycling. The graph also shows greater level of oxidation happening at the BP LCO-LYC interface judging by the larger extent of interfacial resistance growth. While the behaviour of composite cathode is expected based on our prior results, the variation in capacity fade of two LCO crystallography combined with the GITT results (SI 10) sheds more light on the role of cathode morphology and crystallography on interfacial stability.

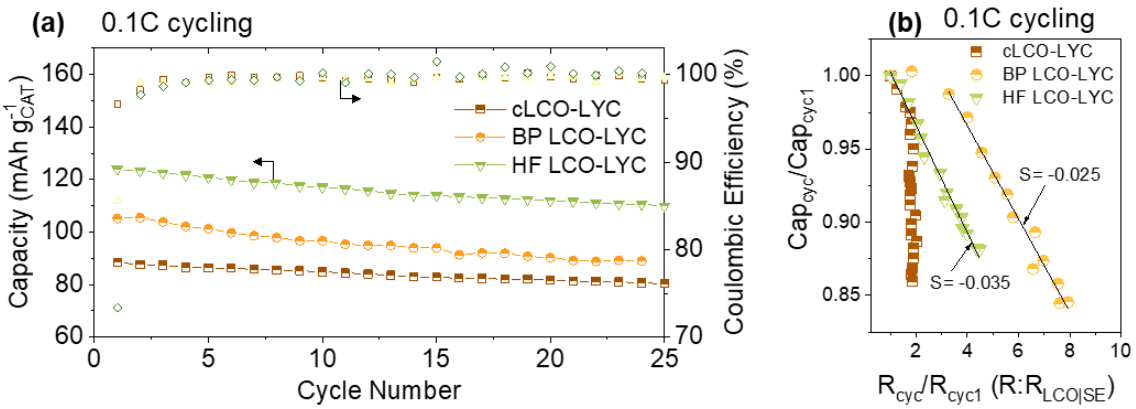

Figure S30. (a) cycling performance of LCO-LYC cells with two LCO orientations compared to that of composite cathodes. All data are collected at 0.1C rate with similar cathode active material loading of 6-7 mg cm^{-2}. (b) master plot of capacity fade vs. increase in interfacial resistance showing the correlation (or lack of) between the two parameters.

SI 11.1.5. Inter-cycling EIS tests: 0.5C cycling

The interface behaviour was investigated at a relatively faster rate 0.5C (C/2) for the most two stable systems, the LCO-LIC composite cathode and HF LCO interfaced with LIC. Figure S31 shows that solid-state cell performance is significantly enhanced when the interface between the cathode and solid electrolyte is limited to a single surface dominated by fast Li-diffusing crystallographic facets. To minimize the sensitivity of capacity retention to overpotential across a possibly resistive interface, the charge-discharge rate was changed to the extremely low rate of 0.02C (C/50) after 84 cycles (Figure 6 (a)). The capacity retention at 0.02C is compared to initial 0.1C values in Figure 31 (b). The results suggest that even a slow rate does not revive the initial capacity in composite cathode as it does for dense LCO-LIC system. Inspection of interfacial resistance (Figure 31 (c)) reveals that cycling at faster rate induces significant change in the composite cathode while dense LCO resistance remains almost constant. The drop of capacitance to half the starting value can also be attributed to increase in the thickness of interfacial layer[27]. It is worth noting that composite cathode capacity retention is still relatively high (85% after 100 cycles relative to first 0.5C cycle) and comparable to that observed in lower rate (0.2C) cycling yet the underlying mechanism of capacity fade might differ. Considering the LIC is electrochemically stable (supported by CV and long-term slow cycling data), we postulate the increase in composite cathode-LIC SE interfacial resistance might be correlated with a combination of formation of an interfacial layer, structural damage to LCO particles and physical interfacial gaps as portrayed by schematics in Figure S32. The nonlinear variation of capacity fade with interfacial resistance (Figure S32) may be indicative of such combined effect and seems to be a typical behaviour of composite cathodes regardless of alkali ion system. Post-mortem microstructural analysis of composite cathode corroborates that structural damage occurs during extended cycling. While the underlying mechanism of capacity fade in composite cathode can include cathode microstructural damage, SE oxidation, formation of resistive cathode-electrolyte interface (CEI) or loss of contact, we have found that it is almost impossible to identify the ones responsible in the performance of a composite cathode.

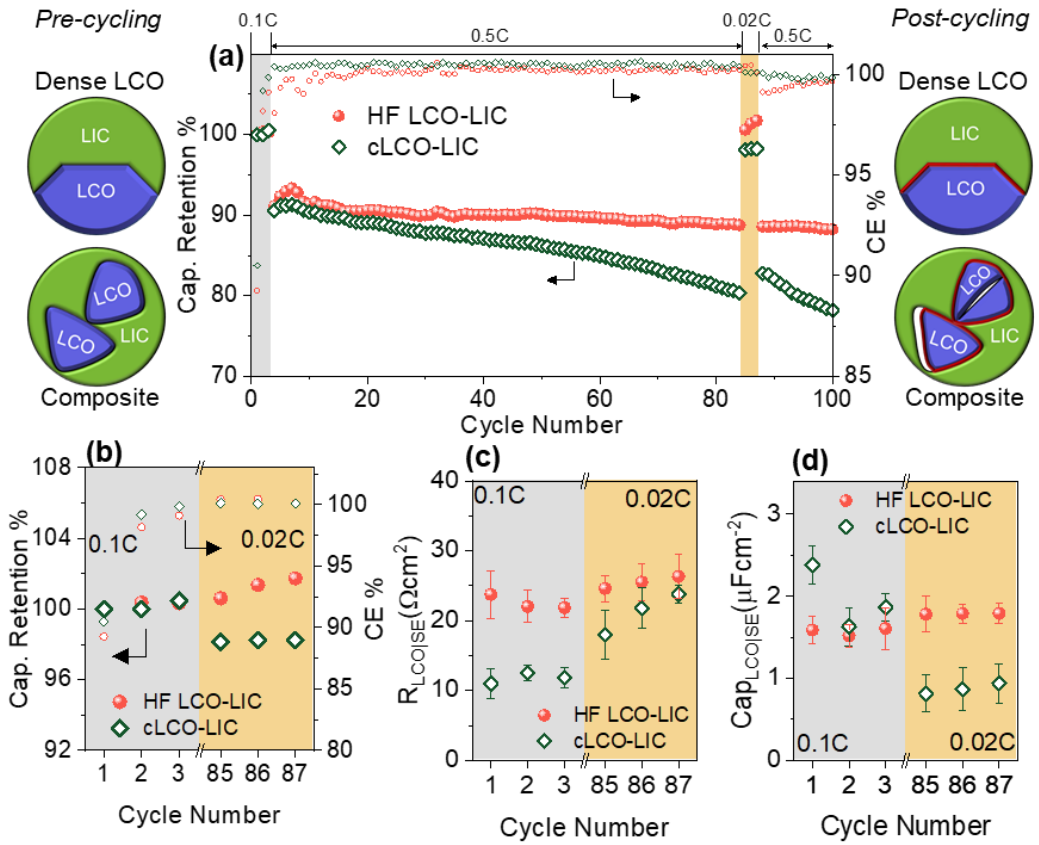

Figure S31. Impact of higher rate cycling for composite and dense LCO with LIC SE. (a) Cycling performance of composite and dense LCO with LIC SE at the relatively fast rate of 0.5C relative to initial capacity at 0.1C (highlighted in grey). Charge-discharge rate is switched to the low rate of 0.02C after 84 cycles (highlighted in orange) to minimize overpotential (kinetic) effects. Comparison of capacity retention (b), interfacial resistance (c) and effective interfacial capacitance (d) before and after cycling measured at slow rates (0.1C initial, 0.02C after 84 cycles) suggests interfacial instability in the composite cathode arises from some combination of a resistive interfacial layer, mechanical damage and physical gap as shown in schematics. Note: interfacial layer is indicated by red line in schematics. Error bars are produced on the basis of three consecutive EIS scans and error analysis of effective capacitance extracted from CPE parameter (see Methods).

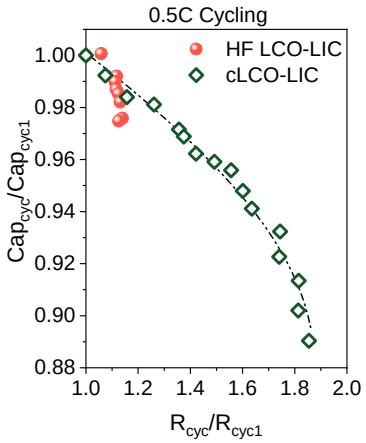

Figure S32. Correlation between capacity fade and increase in interfacial resistance for HF LCO and composite LCO with LIC as the solid electrolyte during fast (0.5C) 80 cycles (starting at cycle 4 and ending at cycle 84 in

Figure S31 of main text). Relative terms are extracted based on values at the initial cycle at 0.5C rate. Dense LCO does not show any correlation between capacity fade and resistance. The capacity of composite cathode varies nonlinearly (indicated by a dashed line) with interfacial resistance.

SI 11.2. Na-ion systems

The interface between SE and NCO cathode was examined by EIS in a similar manner to LCO-SE systems. In the intra-charge test, the cell was charged at 0.1C rate with intermittent resting and EIS profile collection. Figure S33 (a) shows the EIS profiles for a representative dense NCO-NPS as well as NCO-NYZC solid-state cells in the first charge cycle. Figure S33 (b) summarizes the cathode-SE interfacial resistance values as a function of charging voltage. The sulphide SE shows a considerable oxidation at the interface judging by the rapid increase in the interfacial resistance. While all cathodes show similar increasing trend in interfacial resistance with voltage, BP NCO shows the higher values while composite cathode display a mild increase resembling that of composite LCO cathodes. The dashed line shows the theoretical onset of oxidation for NYZC electrolyte beyond which both dense cathodes depict signs of oxidation at interface. The lack of datapoint in the 3.2-3.5 V (vs. Na-Sn) range is due to the vertical jump caused by Na^+ ion - vacancy ordering at the formation of the Na_xCoO_2 (x=0.5) phase[4]. These results highlight again that interfacial analysis of composite cathode structures does not reveal the severity of interfacial reactions upon slight oxidation events. Figure S33 (c) shows the correlation master plot for all the three cathode structures. Similar to the case of LCO-SE, dense cathodes follow the linear relationship between a degree of capacity fading and increase of interfacial resistance. On the other hand, composite cathode displays a nonlinear behaviour similar to the case of fast cycling LCO-LIC in Figure S32. The different behaviour of composite NCO cathode from that of composite LCO-SE in Figure 4 lies in the fact that a larger charge cut-off voltage was used to enhance the oxidation effect. Overall, the linear correlation observed in dense cathode systems offers the possibility of using interfacial resistance as prediction tool for the state of solid-state battery health throughout long term cycling. Our findings with Na ion solid-state systems suggest the universality of the critical role cathode morphology and crystallography in understanding of interfacial stability in solid-state batteries.

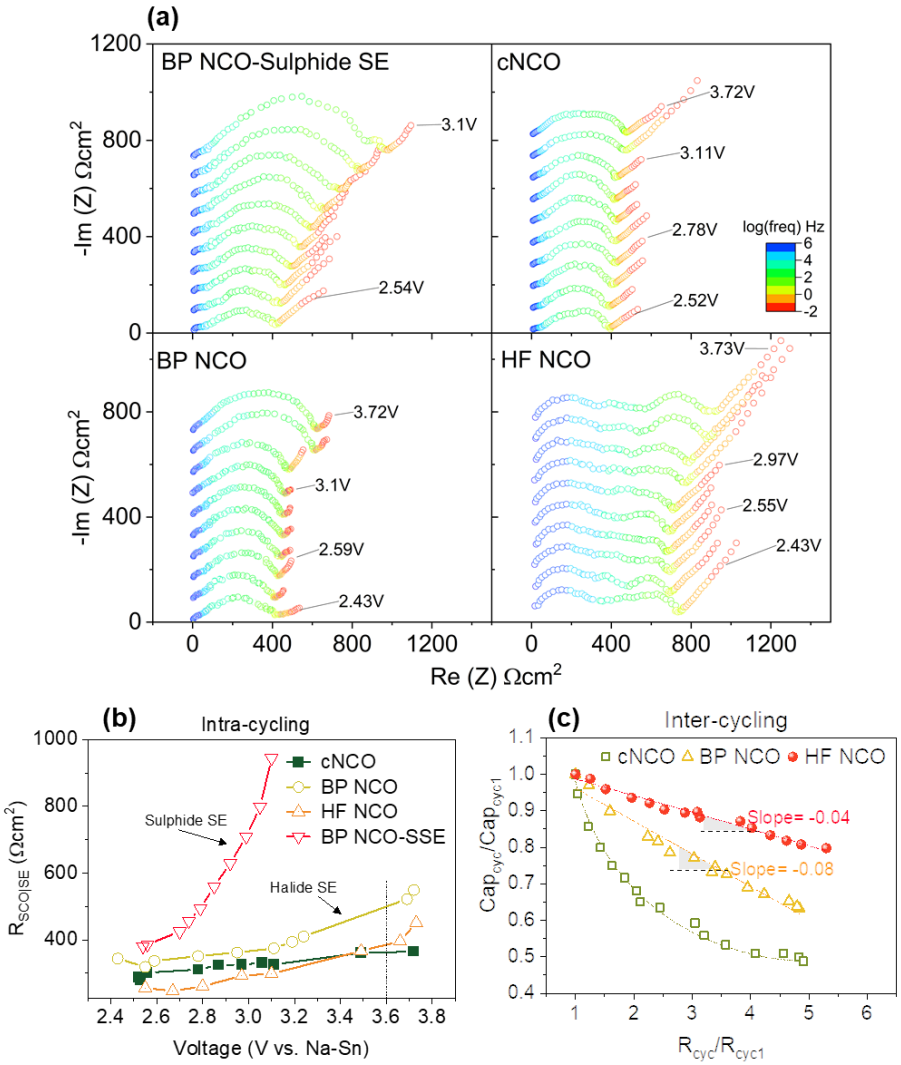

Figure S33. (a) Intra-cycle impedance measurement during the initial charge cycle for composite (cNCO) and dense (BP, HF) NCO cathodes. This top-left graph in (a) shows a representative BP NCO-NPS system without the use of halide NYZC SE. (b) Evolution of cathode-solid electrolyte interfacial resistance as a function of cell voltage for sulphide and halide systems indicating instability in NCO-NPS interface. (c) Master plot demonstrating correlation between capacity fade and interfacial resistance for dense and composite cathodes. Capacity fade and increase in interfacial resistance are shown in relative terms (with respect to first cycle) to enable direct comparison. All tests have been performed at 0.1C rate.

SI 12. Interface Chemistry

Attaining an isolated cathode-SE interface in our dense LCO-SE systems allows for direct XPS investigation of the interface after cycling. The Cl 2p and Y 3d spectra of LCO-LYC systems (Figure S34) shows trace amount of a most likely YCl_3 oxidation product in agreement with our CV measurements and theoretical predations[10]. The chemical state of yttrium remains unchanged (Figure S34) since bonding of Y and Cl are similar in YCl_3 and YCl_6^{3-} octahedra in LYC[5,31]. However, the extra Cl 2p peak doublet shifting to higher energies aligns with higher binding energy of Cl 2p in YCl_3 compared with Cl 2p in LYC[32]. The extent of oxidation seems to be higher for BP LCO in agreement with the poor

performance of this system. In a separate experiment, the two sides of BP LCO-LYC interface were analysed by XPS (Figure S35) which further confirmed the presence of LYC oxidation product most likely contributing to the observed increased impedance (Figure 4). Analysis of Cl 2p and In 3d profiles in the LCO-LIC systems (Figure S36) corroborate the observed higher stability of LIC. No chemical shift is observed in the Cl 2p after cycling with the exception is a small trace of most likely $InCl_3$[32,33] in BP LCO that may support our hypothesis of limited active edges (local high overpotential) promoting SE oxidation. The indium chemical state is in line with expectation of 3+ oxidation state and remains unchanged after cycling[33]. Overall, XPS confirms the superior performance of LIC is due to higher oxidation stability. Moreover, it is evident that XPS analysis of cationic species, i.e. In^{3+} and Y^{3+} do not provide a full understanding of solid electrolyte stability. It seems that evaluation of the anionic species, similar to a recent Li_3ScCl_6-LCO study[8], offers a complimentary and more conclusive picture of interface deterioration during cycling.

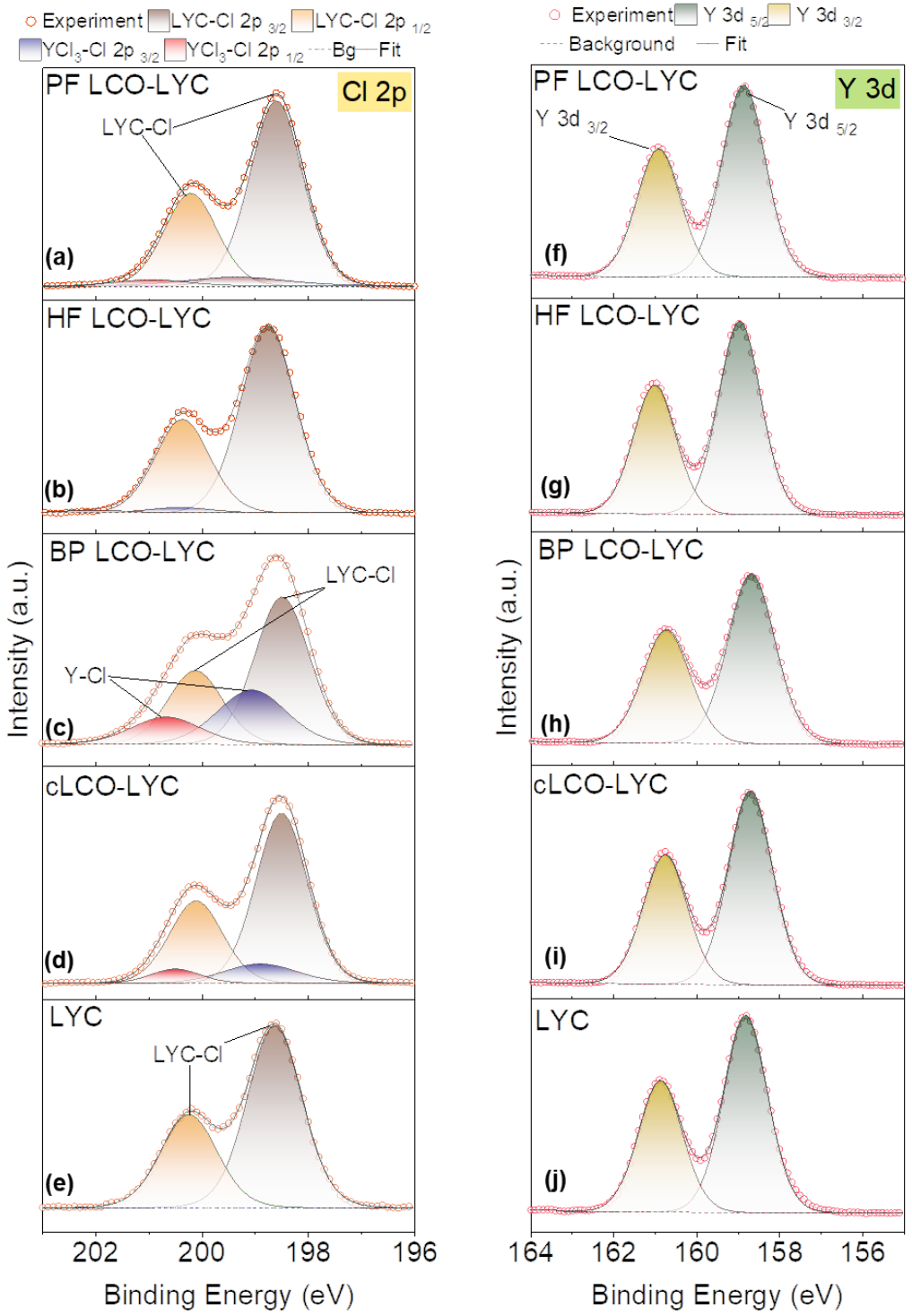

Figure S34. High resolution XPS profiles near (a-e) Cl 2p and (f-j) Y 3d biding energy for LYC related systems.

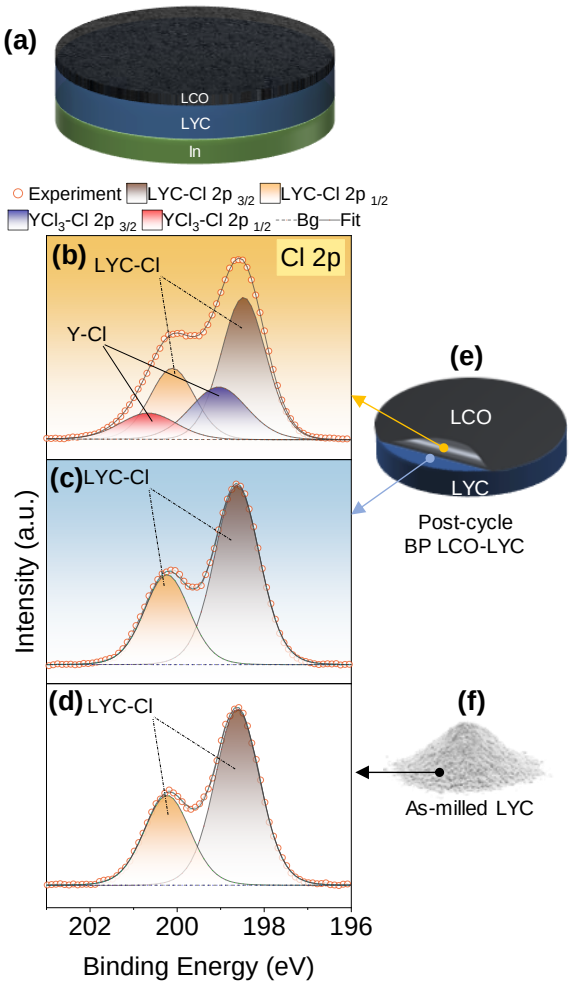

Figure S35. (a) schematic of cell construction for a BP LCO-LYC solid state cell. Cl 2p XPS profiles for regions near the interface on (b) BP LCO cathode and (c) LYC pellet after prolonged cycling as well as initial (d) LYC as-milled powder. (e) shows a schematic of BP LOC layer peeled off the SE (LYC) pellet exposing the two sides of cathode-SE interface. (f) schematic of LYC as-milled powder.

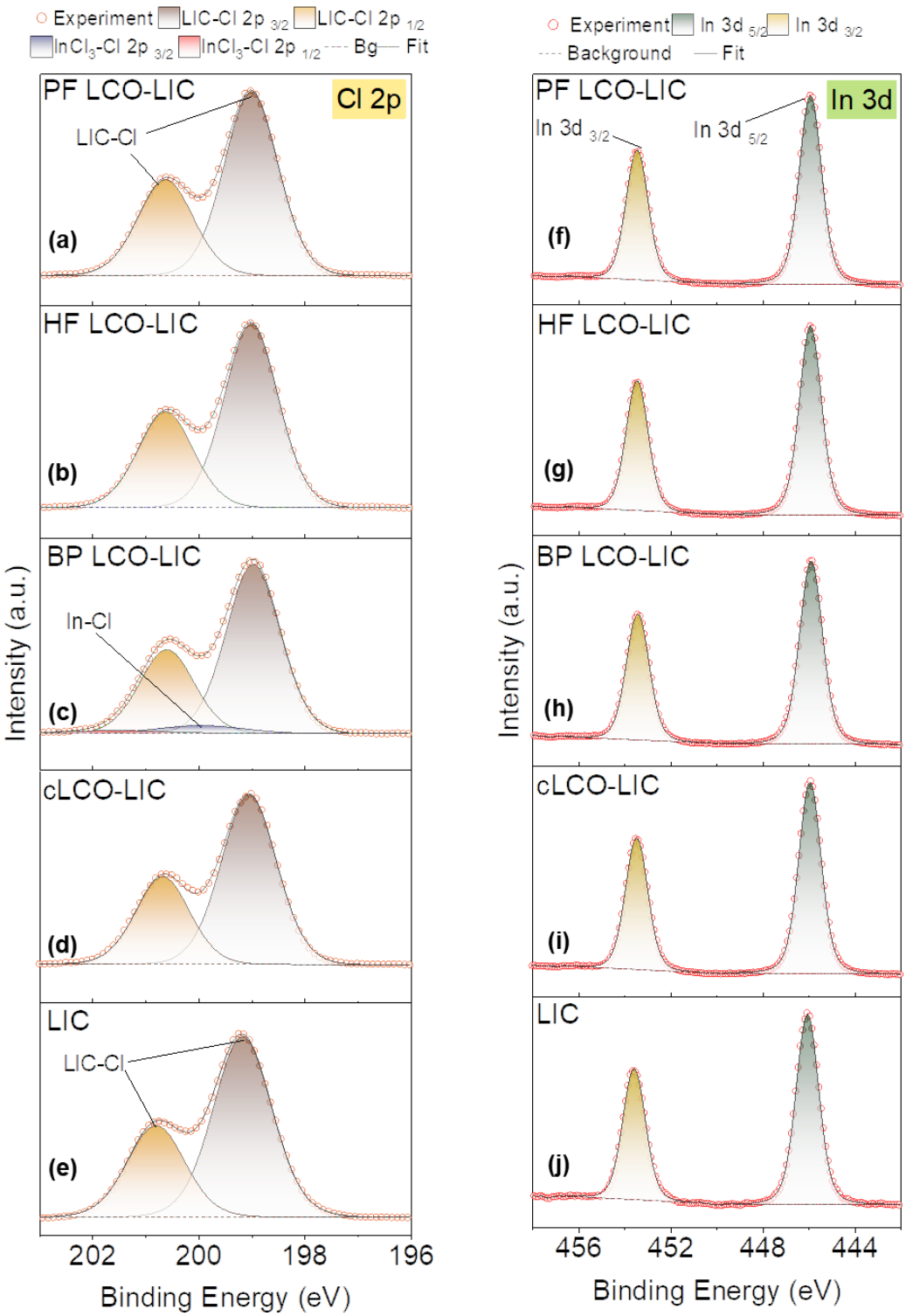

Figure S36. High resolution XPS profiles near (a-e) Cl 2p and (f-j) In 3d biding energy for LIC related systems.

SI 13. Interface Microstructure

Comparing the cross-section morphology of composite cathode before and after extended cycling shows the presence of microcracks. Crack formation seems to occur along basal planes judging by the channelling contrast (ion beam SEM) in Figure S37, in agreement with prior reports[20]. Moreover, cracking tends to appear in large (>10 µm) LCO particles and is absent in smaller particles. Several regions with clear gaps in the LCO-SE interface are also present. The cross-section morphology of all dense LCOs (Figure S38) retains its original structure as well as nanoscale terracing features confirming the mechanical durability under pelletizing conditions. Furthermore, the SE powder seems to have conformed to the surface roughness of the dense LCO surface forming an intimate LCO-SE contact. We did not observe microcracking in these structures. These observations confirm the structure of the electrodeposited LCOs is robust toward fabrication processes and resilient to electrochemical induced defects during prolonged cycling.

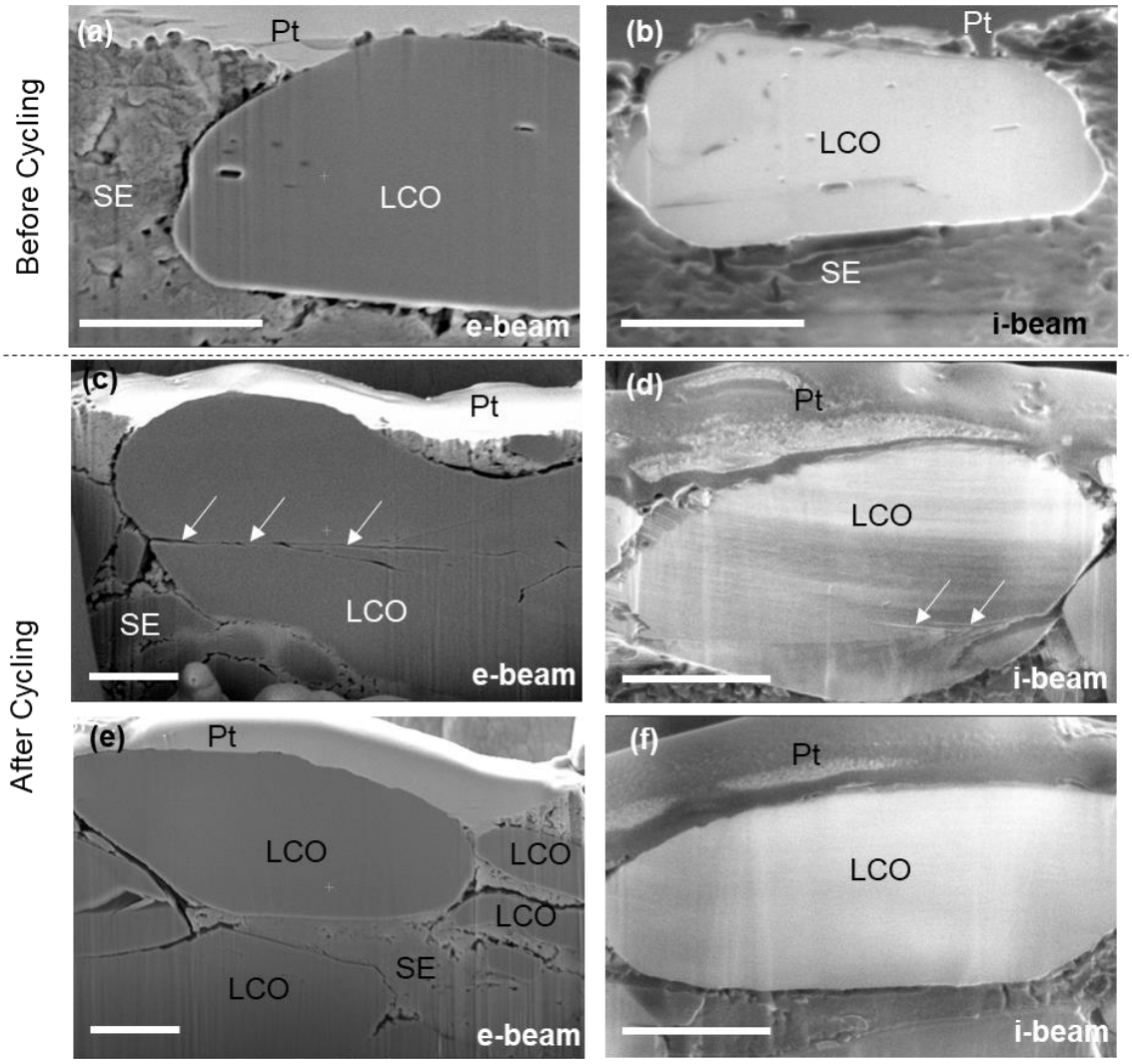

Figure S37. SEM-FIB cross section of (a and b) pre-cycling structure of composite LCO and SE captured by (a) electron beam and (b) Ga ion beam. (c and e) electron beam and (d and f) ion beam SEM micrographs of composite cathode after extended cycling. The channelling contrast in (d) shows the stacking of LCO basal planes. Arrows in

(c) and (d) point to cracks along the <003> direction. (e) and (f) show intact defect-less LCO particles after cycling. SE: LYC and scale bar is 3µm for all micrographs.

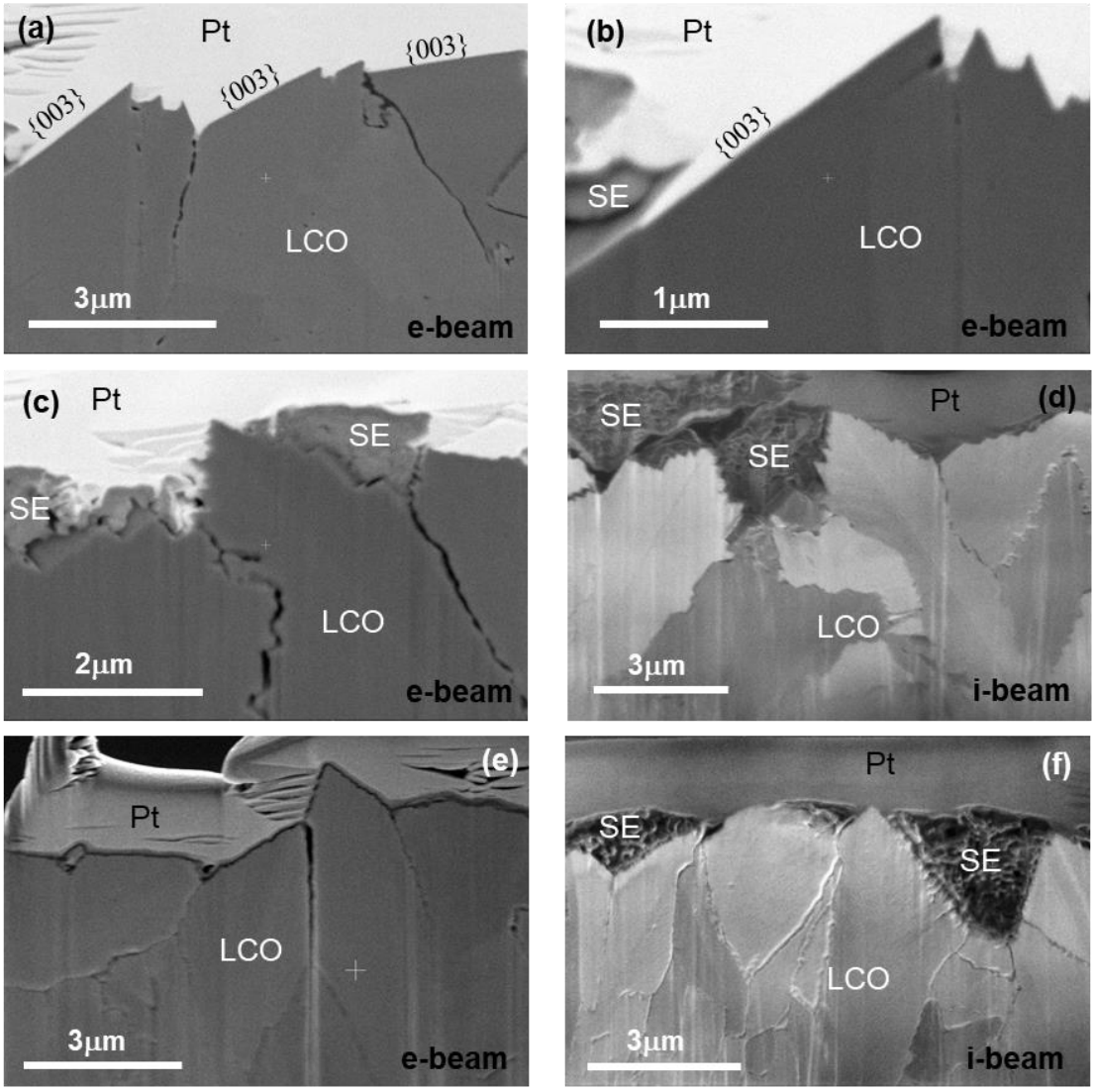

Figure S38. SEM-FIB cross section of (a and b) BP LCO, (c and d) HF LCO and (e and f) PF LCO after the cycling tests. E-beam and i-beam refer to the mode of imaging being conventional electron beam induced SEM and ion beam induced SEM, respectively. SE: LIC.

SI 14. Energy density calculations: composite vs. dense cathode

The gravimetric and volumetric energy densities of SSBs with practical parameters in commercial pouch cells of LCO cathode and different solid electrolytes have been reported for composite cathode structures[9]. Using exact similar assumptions of pouch cell parameters[34,35], and a cathode thickness of 65 µm, dense LCOs are compared to composite cathode mixture of 80 and 90 wt.% active material content in Figure S39. It is worth noting that the compatibility of LIC with respect to Li anode is not considered in these calculations. To achieve 400 Wh kg^{-1} in a typical composite of LCO (80 wt%)-LIC cathode, SE thickness <10 µm is required which is impractical. However, the minimum thickness requirement shifts to 50 µm to reach 400 Wh kg^{-1} when using dense LCOs. This highlights the benefit of using additive-free cathode to build new generation SSBs.

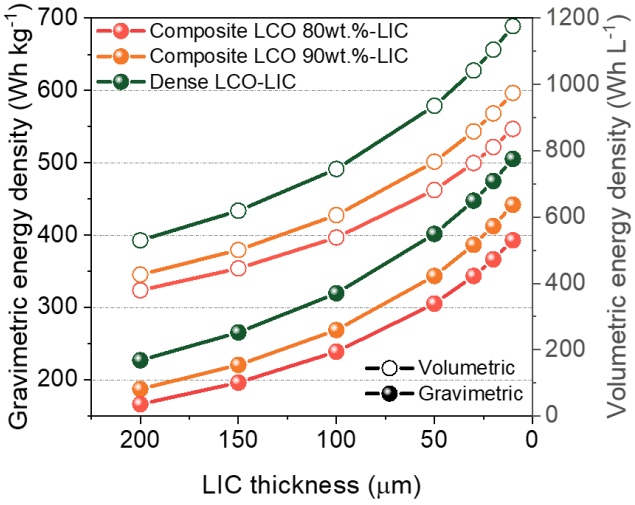

Figure S39. Gravimetric and volumetric energy densities comparison of composite and dense LCO-LIC SSBs in pouch cell (8 layers) configuration.

References

1. Momma, K. & Izumi, F. VESTA 3 for three-dimensional visualization of crystal, volumetric and morphology data. *J. Appl. Crystallogr.* **44**, 1272–1276 (2011).

2. Canovic, S., Jonsson, T. & Halvarsson, M. Grain contrast imaging in FIB and SEM. *J. Phys. Conf. Ser.* **126**, 12054 (2008).

3. Paufler, P. C. S. Barrett, T. B. Massalski.Structure of Metals. 3rd revised edition. Pergamon Press Oxford, New York, Toronto, Sydney, Paris Frankfurt/M 1980 654 Seiten, 113 Abbildungen, 19 Tabellen und über 1400 Literaturhinweise. Preis US $ 20.–. *Krist. und Tech.* **16**, 982–982 (1981).

4. Berthelot, R., Carlier, D. & Delmas, C. Electrochemical investigation of the P2-NaxCoO2 phase diagram. *Nat. Mater.* **10**, 74–80 (2011).

5. Asano, T. *et al.* Solid Halide Electrolytes with High Lithium-Ion Conductivity for Application in 4 V Class Bulk-Type All-Solid-State Batteries. *Adv. Mater.* **30**, 1803075 (2018).

6. Li, X. *et al.* Air-stable Li3InCl6 electrolyte with high voltage compatibility for all-solid-state batteries. *Energy Environ. Sci.* **12**, 2665–2671 (2019).

7. Li, X. *et al.* Water-Mediated Synthesis of a Superionic Halide Solid Electrolyte. *Angew. Chemie* **131**, 16579–16584 (2019).

8. Liang, J. *et al.* Site-Occupation-Tuned Superionic LixScCl3+x Halide Solid Electrolytes for All-Solid-State Batteries Site-Occupation-Tuned Superionic Li x ScCl 3+x Halide Solid Electrolytes for All-Solid-State Batteries. (2020) doi:10.1021/jacs.0c00134.

9. Li, X. *et al.* Progress and perspectives on halide lithium conductors for all-solid-state lithium batteries †. (2020) doi:10.1039/c9ee03828k.

10. Wang, S. *et al.* Lithium Chlorides and Bromides as Promising Solid-State Chemistries for Fast Ion Conductors with Good Electrochemical Stability. *Angew. Chemie Int. Ed.* **58**, 8039–8043 (2019).

11. Zhang, Z. *et al.* New horizons for inorganic solid state ion conductors. *Energy and Environmental Science* vol. 11 1945–1976 (2018).

12. Han, F., Zhu, Y., He, X., Mo, Y. & Wang, C. Electrochemical Stability of $Li_{10}GeP_2S_{12}$ and $Li_7La_3Zr_2O_{12}$ Solid Electrolytes. *Adv. Energy Mater.* **6**, 1501590 (2016).

13. Hayashi, A., Noi, K., Sakuda, A. & Tatsumisago, M. Superionic glass-ceramic electrolytes for room-temperature rechargeable sodium batteries. *Nat. Commun.* **3**, 1–5 (2012).

14. Nguyen, H. *et al.* Single-step synthesis of highly conductive Na3PS4 solid electrolyte for sodium all solid-state batteries. *J. Power Sources* **435**, 126623 (2019).

15. Wu, E. A. *et al.* A stable cathode-solid electrolyte composite for high-voltage, long-cycle-life solid-state sodium-ion batteries. *Nat. Commun.* **12**, 1256 (2021).

16. Zhang, H. *et al.* Electroplating lithium transition metal oxides. *Sci. Adv.* **3**, e1602427 (2017).

17. Takeuchi, S. *et al.* Epitaxial LiCoO2 films as a model system for fundamental electrochemical studies of positive electrodes. *ACS Appl. Mater. Interfaces* **7**, 7901–7911 (2015).

18. Reimers, J. N. Electrochemical and In Situ X-Ray Diffraction Studies of Lithium Intercalation in Li[sub x]CoO[sub 2]. *J. Electrochem. Soc.* **139**, 2091 (1992).

19. Reimers, J. N. Effects of Impurities on the Electrochemical Properties of LiCoO[sub 2]. *J. Electrochem. Soc.* **140**, 2752 (1993).

20. Zhang, W. *et al.* Degradation Mechanisms at the Li10GeP2S12/LiCoO2 Cathode Interface in an All-Solid-State Lithium-Ion Battery. *ACS Appl. Mater. Interfaces* **10**, 22226–22236 (2018).

21. Kalluri, S. *et al.* Surface Engineering Strategies of Layered LiCoO2 Cathode Material to Realize High-Energy and High-Voltage Li-Ion Cells. *Adv. Energy Mater.* **7**, 1601507 (2017).

22. Park, K. H. *et al.* High-Voltage Superionic Halide Solid Electrolytes for All-Solid-State Li-Ion Batteries. *ACS Energy Lett.* 533–539 (2020) doi:10.1021/acsenergylett.9b02599.

23. Wu, E. *et al.* A Stable Cathode-Solid Electrolyte Composite for Long-Cycle-Life, High Voltage Solid-State Sodium-ion Batteries. (2020) doi:10.26434/CHEMRXIV.12730964.V1.

24. Lei, Y., Li, X., Liu, L. & Ceder, G. Synthesis and stoichiometry of different layered sodium cobalt oxides. *Chem. Mater.* **26**, 5288–5296 (2014).

25. Groen, C. P., Oskam, A. & Kovács, A. Theoretical Study of Mixed $MLaX_4$ (M = Na, K, Cs; X =

F, Cl, Br, I) Rare Earth/Alkali Metal Halide Complexes. *Inorg. Chem.* **42**, 851–858 (2003).

26. Shiraki, S. *et al.* Atomically Well-Ordered Structure at Solid Electrolyte and Electrode Interface Reduces the Interfacial Resistance. *ACS Appl. Mater. Interfaces* **10**, 41732–41737 (2018).

27. Zhang, W. *et al.* Interfacial Processes and Influence of Composite Cathode Microstructure Controlling the Performance of All-Solid-State Lithium Batteries. *ACS Appl. Mater. Interfaces* **9**, 17835–17845 (2017).

28. Sakuda, A., Kitaura, H., Hayashi, A., Tadanaga, K. & Tatsumisago, M. Modification of Interface Between LiCoO2 Electrode and Li2S – P2S5 Solid Electrolyte Using Li2O – SiO2 Glassy Layers. *J. Electrochem. Soc.* **156**, A27 (2009).

29. Kim, J., Kim, M., Noh, S., Lee, G. & Shin, D. Enhanced electrochemical performance of surface modified LiCoO2 for all-solid-state lithium batteries. *Ceram. Int.* **42**, 2140–2146 (2016).

30. Wang, D. *et al.* Mitigating the Interfacial Degradation in Cathodes for High-Performance Oxide-Based Solid-State Lithium Batteries. *ACS Appl. Mater. Interfaces* **11**, 4954–4961 (2019).

31. Templeton, D. H. & Carter, G. F. The crystal structure of yttrium trichloride and similar compounds. *J. Phys. Chem.* **58**, 940–944 (1954).

32. Naumkin, A. V, Kraut-Vass, A., Gaarenstroom, S. W. & Powell, C. J. NIST X-ray photoelectron spectroscopy database, version 4.1. *Natl. Inst. Stand. Technol. Gaithersbg.* (2012).

33. Freeland, B. H., Habeeb, J. J. & Tuck, D. G. Coordination compounds of indium. Part XXXIII. X-Ray photoelectron spectroscopy of neutral and anionic indium halide species. *Can. J. Chem.* **55**, 1527–1532 (1977).

34. Liu, L. *et al.* Practical evaluation of energy densities for sulfide solid-state batteries. *eTransportation* **1**, 100010 (2019).

35. Gao, Z. *et al.* Promises, Challenges, and Recent Progress of Inorganic Solid-State Electrolytes for All-Solid-State Lithium Batteries. *Advanced Materials* vol. 30 1705702 (2018).